Journal of Hydrology: Regional Studies 63 (2026) 103025

Contents lists available at ScienceDirect

Journal of Hydrology: Regional Studies

journal homepage: www.elsevier.com/locate/ejrh

A revisit of Niger river's major flood events and the role of convective systems with satellite data and hydrological modeling

Fatou Josiane Guehi [a,b,*], Rômulo Augusto Jucá Oliveira [c], Marielle Gosset [b], Modeste Kacou [a], Eric-Pascal Zahiri [a], Thomas Fiolleau [d]

[a] Laboratoire des Sciences de la Matières, de l'Environnement et de l'Energie Solaire (LASMES), Université Félix Houphouët-Boigny, Abidjan 01 BPV 34, Côte d'Ivoire
[b] Géoscience Environnement Toulouse, GET, IRD, CNRS, CNES, Université de Toulouse, 14 avenue Ed. Belin, Toulouse 31400, France
[c] Hydro Matters, 1 Chemin de la Pousaraque, Le Faget 31460, France
[d] Laboratoire d'Etudes en Géophysique et Océanographie Spatiales (CNRS/CNES/IRD/UPS),Université de Toulouse, Toulouse, France

ARTICLE INFO

Keywords:
Niger river
Rainfall
Satellite
Floods
Extreme events
Mesoscale convective systems

ABSTRACT

Study region: The study focuses on the Niger river in West Africa.
Study focus: The impact of tropical convection on extreme phenomena like the recurrent floods of the Niger river in Niamey is analyzed. A new method based on meteorological satellite data and hydrological modeling is used to analyze the intersection between the trajectory of the storms and the hydrological basin. The total volume of rain brought by each mesoscale convective system (MCS) crossing the water shed is quantified. The method is applied to decompose the hydrograph of the Niger river in Niamey and highlight the impact of the major rain events on the record flood of 2020.
New hydrological insights for the region: The role of the MCSs crossing the subbasins contributing to the phenomena of the red flood in Niamey is highlighted. The 10 MCS that brought the largest volumes of rain over the area explain about 50 % of the discharge peak that lead to serious flooding in 2020. The rainiest MCS caused a rise of about 17 % with a lasting effect over more than a week. These figures illustrate that detecting major MCSs and quantifying the associated rain volume could help in flood prediction in a region very impacted by these phenomena.

1. Introduction

Over the past two decades, floods have accounted for 44 % (the largest percentage) of all disasters, affecting 1.6 billion people worldwide (CRED-Disaster-Report-Human-Cost2000-2019.pdf–2019.pdf.pdf, n.d.). In West Africa, for example, flooding caused by torrential rains in September 2009 affected over 600,000 people, mainly in Ghana and the Sahelian countries of Senegal, Burkina Faso and Niger (Di Baldassarre et al., 2010). Flood damage continues to increase, and the risk of flooding is set to almost double by 2100, even under projections based on the most optimistic global warming scenarios (Alfieri et al., 2017). It is therefore essential to find sustainable solutions for flood planning and protection in urban environments and on a catchment scale. An important step in this process of finding solutions is flood risk assessment and better understanding of the physical processes in flood genesis. Many

* Corresponding author at: Laboratoire des Sciences de la Matières, de l'Environnement et de l'Energie Solaire (LASMES), Université Félix Houphouët-Boigny, Abidjan 01 BPV 34, Côte d'Ivoire.
E-mail addresses: fatoujosiane.guehi@ird.fr, josifat1989@gmail.com (F.J. Guehi).

https://doi.org/10.1016/j.ejrh.2025.103025
Received 16 August 2025; Received in revised form 3 December 2025; Accepted 6 December 2025
Available online 12 December 2025

researches have focused on rainfall intensification and land use change as sources of flood risk enhancement (e.g. Aryee et al., 2024; Casse et al., 2016; Hirabayashi et al., 2008). A common conclusion of these studies is that changes in precipitation characteristics and land use influence historical flooding trends.

In the Sahel, most of the annual precipitation is provided by the West African monsoon flow, associated with the northward migration, during the boreal summer, of the Intertropical Convergence Zone (ITCZ), where this humid monsoon flow meets the Harmattan, the hot, dry air coming from the Sahara (Geen et al., 2020; Janicot et al., 2011). This period, from June to September, corresponds to the monsoon or rainy season. In this region, the intense precipitation that occurs is mainly the result of Mesoscale Convective Systems (MCSs) (Mathon et al., 2002), whose formation is favored by the atmospheric conditions induced by the northward shift of the ITCZ during the rainy season (e.g. Biasutti, 2019). The importance of these organized systems in the amount of precipitation produced in the tropics has been widely studied (e.g. Mathon et al., 2002; Prein et al., 2023; Roca and Fiolleau, 2020; Zahiri et al., 2016). According to Roca et al., (2024), a considerable shift in the frequency of deep convective cloud systems' occurrences, especially due to an increase of relatively small and long-lived cloud systems, have been observed over the last three decades over continental Africa and the Atlantic Ocean. Future projections suggest that with global warming, which is expected to reach + 4 to + 5 ° by 2100 if greenhouse gas emissions are not reduced (Calvin et al., 2023, "IPCC"), convection within MCSs should intensify with a significant increase in extreme (hourly and daily) precipitation (Taylor et al., 2017; Klein et al., 2021; Zhao, 2022; Bao et al., 2024). For example, Klein et al., 2021 exploited changes in wind shear and total water column content in the atmosphere to simulate, in climate models, extreme precipitation associated with MCSs in the Sahelian region. An average increase of 26 % between 2030 and 2060, and of 55 % between 2070 and 2100, in extreme hourly precipitation associated with MCSs was highlighted under the most pessimistic warming scenario RCP8.5.

In view of this intensification of MCSs, a number of studies have examined rainfall patterns and the contribution of MCSs to rainfall

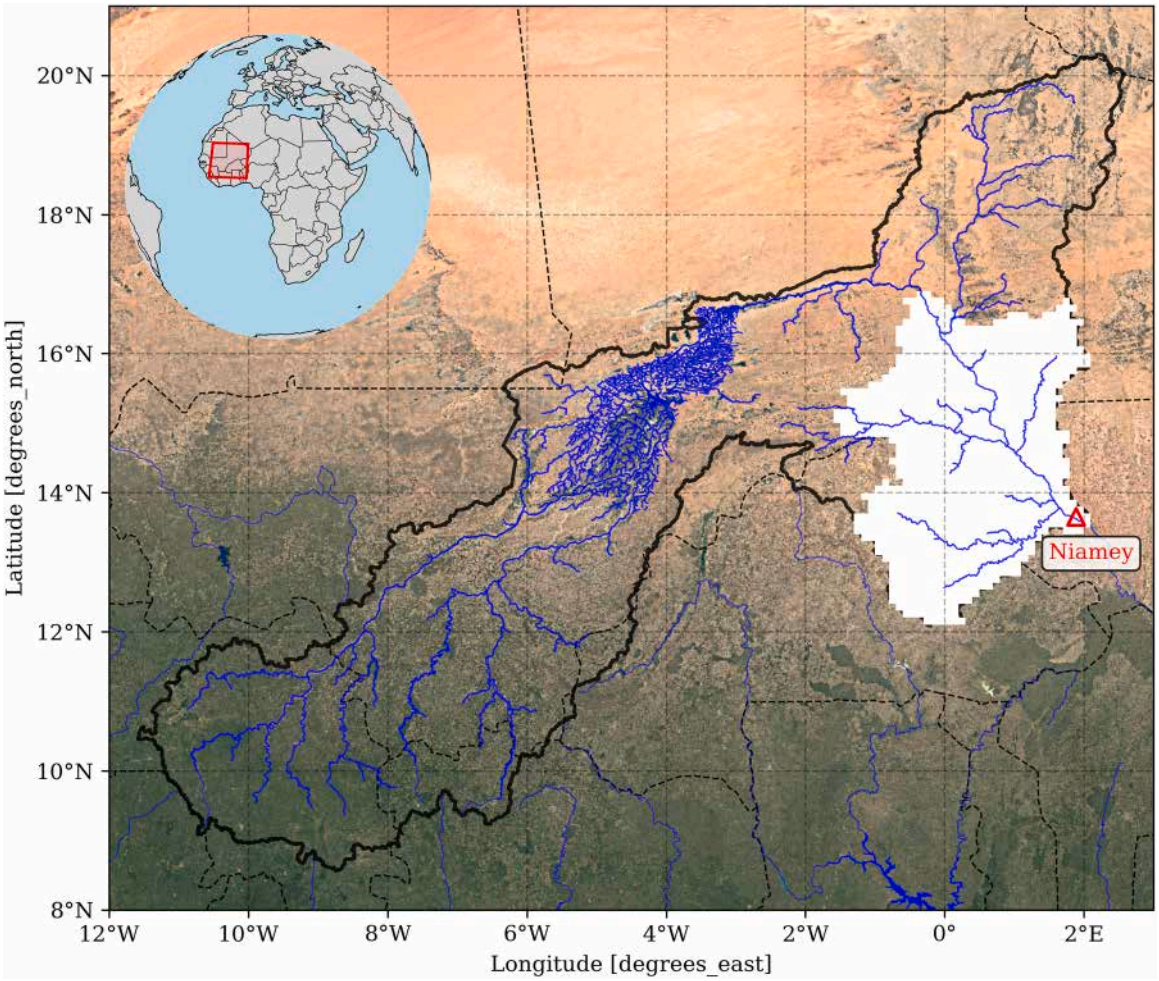

Fig. 1. The study region with, in black, the contours of the Upper and middle Niger river basin, up to the city of Niamey (red triangle), as indicated. The white background highlights the area where the runoff contributes to the genesis of the red flood of the Niger river in Niamey, which is of special interest for this study. The blue lines follow the hydrographic network, showing a high density of lines in the Niger Inner Delta (around 4° W; 15° N).

flooding in tropical regions. Atiah et al. (2023) have related reported flood cases in the South of West Africa between 2015 and 2019 and the rainfall event that caused them, highlighting the role of MCSs. Ding et al. (2024) carried out an exhaustive statistical study where they have related floods reported by the Darthmouth Flood Observatory (DFO) database to the characteristics of MCSs, using an attribution algorithm for a 22-year period.

Most of these previous studies are based on a statistical approach rather than analyzing the physical processes that lead from individual storms to flooding. Most have concentrated on the role of MCSs in flood events due to rainfall that occurred in the neighborhood or directly above the flooded area; this is typically the case for urban flooding (or other flash flood type phenomena). The analysis of the spatio-temporal distribution of the rainfall associated with individual storms and its integration by the basin has not been addressed.

The objective of the present work is to analyze the role of individual storms in the genesis of strong rises in the discharge that could lead to flooding. We propose an original approach for quantifying the impact of individual MCSs on the river hydrological response. We use a fully distributed hydrological model to integrate in space and time the rainfall produced by individual MCSs as they cross a given watershed. The trajectory of the storms and the rainfall they produce are obtained from satellite products. This combined observation and modeling approach is used to revisit and better understand the genesis of some of the major flood events that occurred over the Niger basin. In the last years, the capital of Niger, Niamey has suffered several cases of floods related to extreme events. An absolute record was reached in 2020. That year, the rise in water levels was rapid compared with previous years. In just two days, the river flow in Niamey rose from 1457 m3/s on 06/08/2020–2159 m3/s on 08/08/2020 (ABN, 2021). In September 2020, the Niamey region recorded 61,009 disaster victims. The damage recorded was particularly severe in this area, which until then had not been among the worst hit (Niger Rapport de situation, 2020).

The work presented in this paper is organized as follows: Section 2 presents the hydrological context of the Niger river basin and the flood dynamics in Niamey. Section 3 describes the satellite datasets used to analyze the MCSs trajectories and rainfall. Section 4 describes the hydrological model and its ability to simulate the discharge of the Niger River in Niamey. The method used to isolate the contribution of each MCS into the hydrological simulation is detailed in Section 5. Section 6 presents a hydrometeorological revisit of the record floods that occurred in Niamey in 2020. The particularities of the 2020 rainy season and the characteristics of the major MCSs are analyzed. The hydrological impact of the MCSs that led to record discharge that year is highlighted using the satellite data and hydrological modeling. The main findings are presented in Section 7.

2. Hydroclimatic context and study area

The study focuses on the middle Niger river basin, a region which has been the subject of many studies because it experienced drastic hydroclimatic changes over the last decades and recurring flooding in the last years (Casseé et al. 2015, 2016; Descroix et al., 2018, 2013; Panthou et al., 2014, Sighomnou et al., 2013). These changes have been well illustrated by the evolution of the River's

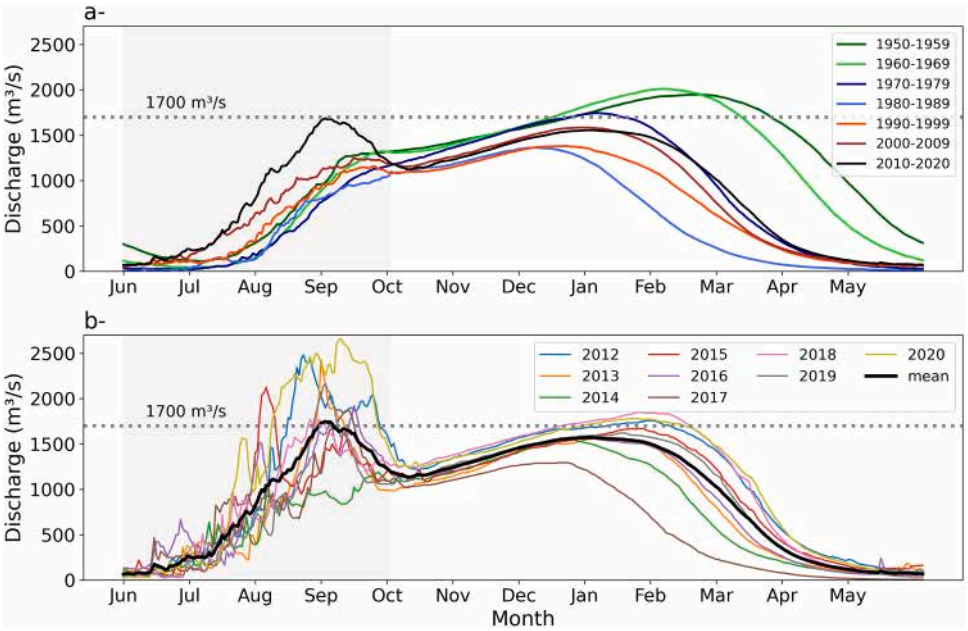

Fig. 2. (a) Decadal mean hydrographs of the Niger River at Niamey over 7 decades (1950–2020). (b) Annual hydrographs of the Niger River at Niamey from 2012 to 2020, the 9-year mean hydrograph is shown in black. A hydrological year begins on June 1 and ends on May 31 of the following year. The red flood occurs between June and October (period highlighted by the grey background). The discharge data was provided by the ABN (2021).

discharge in the city of Niamey (Niger's capital city). Fig. 1 displays the contours of our focus region which includes the upper and middle Niger river basin from its source down to Niamey. Descroix et al. (2012) have described how the river's hydrograph in Niamey has been gradually transformed over time, from a single main flood during most of the 20th century to a double flood since the 2000s. The shape evolution and the interannual variability of the Niger's hydrograph are illustrated in Fig. 2. The first flood of the Niger river, known as the red or local flood, occurs during the rainy season between August and September. This flood is mainly due to inflows from the right-bank tributaries Gorouol, Sirba and Dargol (Casse et al., 2015; Sighomnou et al., 2013) which have their source in Burkina-Faso. This area is highlighted in white in Fig. 1. The red flood is influenced by precipitation generated by MCSs crossing the highlighted white zone. The second flood, commonly known as the Guinean flood, is initiated in the upper part of the basin. Considerably weakened and delayed by the very gentle slopes of the region it crosses (inner delta, with dense hydrographic network as seen in blue in Fig. 1), its flow into the Middle Niger, near Niamey, is only visible after the rainy season, between November and March (Descroix et al., 2012).

Fig. 2a, displays the mean decadal hydrographs over the period 1950–2010 and shows that the Guinean flood was for a long time more important than the first flood during the wet years (50s-60s), with a single peak occurring in March. Although this peak declined significantly during the decades of severe drought (70–80s), the Guinean flood remained pre-eminent. With the return of rainfall to the Sahelian region in the late 1990s, the first flood (also known as the local or red flood) intensified, considerably surpassing the Guinean flood during the decade 2010–2020. Over the period 2012–2020, during the red flood, the critical flood threshold (1700 m3/s, according to the Niger Basin Authority: ABN) was reached or exceeded in every year except 2014. The highest peak flow values were recorded in 2012, 2013 and 2020 (Fig. 2b). These threshold exceedances during red flood periods lead to frequent inundations in the region. According to several authors (e.g. Descroix et al., 2018, 2013; Panthou et al., 2014, Sighomnou et al., 2013), the increase in extreme precipitation in the Sudano-Sahelian region is one of the direct causes of this intensification and increased frequency of red floods. These extreme precipitation events are associated with the intensification of MCSs caused by global warming (Taylor et al., 2017).

In this paper we focus on the role of MCSs in the intensity of the red flood and especially the record flood that occurred in 2020. The area of interest - shown in white in Fig. 1- is the rainwater drainage area responsible for the Niger River's red flood observed in Niamey (Casse et al., 2015). This region is characterized by a semi-arid tropical area, with two distinct seasons depending on the position of the Inter-Tropical Convergence Zone (ITCZ): a dry period from October to May, and a rainy period from June to September (JJAS), corresponding to the monsoon season and producing between 400 and 600 mm/year. During the rainy season (monsoon season), when the red flood occurs, up to 90 % of total recorded rainfall is produced by the MCSs (Goyens et al., 2012; Mathon et al., 2002; Mohr, 2004).

3. Data

Two types of satellite data are used to analyze the rainfall systems over the region of interest: (i) the Tracking Of Organized Convection Algorithm using a 3 dimensional segmentatioN (TOOCAN) product, based on geostationary satellite data, provides detailed information on individual MCSs and their trajectories along their life cycle, and (ii) precipitation estimates from the Integrated Multi-satellitE Retrievals for Global Precipitation Measurement, version 6 (IMERG V06) for quantifying rainfall each 30 min.

3.1. TOOCAN data

The MCSs, above the study area, were identified and tracked by the TOOCAN algorithm. This algorithm, fully detailed in Fiolleau and Roca (2013) considers a three-dimensional stack of IR images and applies a multi-threshold technique to delineate a spatio-temporal volume associated with deep convection. TOOCAN defines an MCS as a convective core with a cold brightness temperature, associated with a stratiform part with a warmer brightness temperature in the spatio-temporal domain. Groups of adjacent pixels in the IR image (from geostationary satellites) with a temperature below a first threshold of 190 K are identified: this is the convective core detection step. Each newly detected core is assigned a unique label and is not matched to any other. Next, the detected convective cores propagate towards the boundaries of the cold cloud shield, identified at 195 K. The iterative process continues in the same way, with a detection step of 5 K, and stops when the boundaries of the cold cloud shield reach the usual brightness temperature threshold of 235 K. The cloud shield defined, in the space-time domain, by a threshold of 235 K is thus decomposed into several MCSs, by the TOOCAN algorithm. This method solves the merging and splitting problems encountered in algorithms using the zone overlap method. The representation of the MCSs life cycle is improved and convective cells are tracked from initiation to dissipation. In our study, we use version 08 of TOOCAN (Fiolleau and Roca, 2024). In this version, the detection step used is 2 K from 190 K to 235 K. Folleau and Roca (2013;2024) have demonstrated that small detection steps enable convective cores to be detected more accurately and characterized more precisely, with a good detection of the smallest convective systems. TOOCAN offers global coverage of tropical areas, with a horizontal resolution of 4 km and a temporal resolution of 30 min. Physical (e.g. minimum brightness temperature), dynamic (e.g. velocity), morphologic (e.g. size) characteristics of identified MCSs each 30 min, along their life cycle are saved in an output file.

3.2. IMERG satellite rainfall product

Developed as part of the Global Precipitation Measurement (GPM) program, the Integrated Multi-satellite Retrievals for GPM (IMERG, Huffman et al., 2019) algorithm compiles data from a constellation of satellites. This satellite constellation includes the GPM

core observatory, which has two on-board sensors: the Dual-frequency Precipitation Radar (DPR) and the GPM Microwave Imager (GMI), which are based on active and passive microwave (PMW) sensors, respectively. Other Low-Earth Orbit (LEO) satellites, equipped with passive microwave (PMW) sensors, are also part of the GPM constellation (e.g., Megha-Tropiques, AMSR-2 and SSMI/S). GPM precipitation products also consider (infrared (IR) observations from geostationary satellites, maintained by other international agencies (e.g., Meteosat Second Generation (MSG) from EUMETSAT). This multi-satellite approach fills the spatial and temporal gaps left by individual observations. PMWs provide more accurate Level 2 (L2) precipitation estimates from LEO satellites; but, their spatial resolution is relatively coarse and their observation frequency low (every 3 h on average). IMERG Level 3 (L3) provides rainfall estimates on a regular spatial grid of 0.1° grid and a time step of 30 min, by interpolating and merging observations from these different satellites. The IMERG product is available in three latencies: Early Run, Late Run and Final Run. In this study, we use the Final run product (IMERG.F V06) available 3.5 months after observation. This product provides precipitation calibrated with monthly gauge data from Global Precipitation Climatology Center Full and Monitoring products (GPCC, Schneider et al., 2014) and because of its higher quality is recommended for research applications.

Earlier versions of IMERG were assessed over the Sahelian region. Gosset et al. (2018) tested, over a period of 2 years, the three latencies without gauge correction of version 3 of IMERG, at three sites in West Africa (Benin, Niger and Burkina Faso) where high density rain gauges networks were available. The final run of IMERG, then in the process of stabilization was judged to be very encouraging, with R^2 coefficients of 0.66, 0.75 and 0.59 obtained respectively on the Benin, Burkina and Niger sites. For the purposes of our study, the results obtained by Gosset et al. (2018) were updated, over a longer period-from 2012 to 2020-and using IMERG V06 Final run with gauge correction. IMERG daily rainfall estimates were compared with daily accumulations of in-situ measurements from the network of rain gauges of the "Analyse Multidisciplinaire de la Mousson Africaine - Couplage de l'Atmosphère Tropicale et Cycle Hydrologique" observatory (AMMA-CATCH, Lebel et al., 2009) over the square degree of Niamey in Niger. The comparisons between the product and the gauges were done by selecting pixels with at least 1 gauge inside, in the area of interest. The main results for rainfall estimation considering all the MCSs during the 9 years are shown in Table 1. For the entire 2012–2020 period, the coefficient of determination R^2 is 0.6 and the relative bias on daily mean rainfall is 1.7 %. The high correlations demonstrate the good ability of the product to capture the dynamics of rainfall at the daily scale, which is important for hydrology. The overall bias is very low. The results compared to Gosset et al. (2018) confirm the improvement of IMERG's successive versions, with a reduction of bias in particular.

4. Hydrological modeling

4.1. Model description

River Niger discharges were simulated using the large-scale semi-distributed rain-discharge hydrologic-hydrodynamic model MGB ("Modelo de Grandes Bacias" in Portuguese or "Large Basins Model" in English) (Collischonn et al., 2007; Pontes et al., 2017). This model, developed for the study of large basins, subdivides the studied watershed into several interconnected unit-catchments, also called mini-basins, which are derived from high resolution DEMs (Digital Elevation Models). The discretization process begins by dividing the hydrographic network into 10 km river sections. Next, the contributing areas around each river section are delineated: these are the elementary water balance calculation units, or mini-basins. Each mini-basin is made up of several Hydrological Response Units (HRUs), which are zones with homogeneous hydrological characteristics. These HRU zones are delimited using satellite information on land use, soil types and vegetation. Once the subdivision process has been completed, the soil water balance is calculated for each HRU in the mini-basin, and the flow generated by these different HRUs is routed to the waterway and then to the river network (Pontes et al., 2022). As a main input variable for the model, daily rainfall data are used as forcing for discharge simulation. The model is suited for using high resolution gridded precipitation products, either from in-situ (interpolated) observations or from satellite data. This is particularly beneficial for tropical regions which often have a low density of rain gauges (Kidd et al., 2017). The MGB model has already been applied in several major tropical basins, including South America (e.g. Siqueira et al., 2018), the Congo River basin (Paris et al., 2022; Wongchuig et al., 2023) and the upper Niger River basin (Fleischmann et al., 2018). In addition, MGB continues to evolve with various physical and numerical implementations, which include the assimilation of satellite altimetry data, as well as the improved representation of lakes and dams (Wongchuig et al., 2023). MGB has also been used operationally to monitor/predict discharges at any point on the river in the Niger (https://mgb-hyfaa.pigeo.fr/) and Guyana (https://sagui.hydro-matters.fr/) watersheds using the near-real-time (NRT) multi-platform rainfall product (with gauge adjustment) Global Satellite Mapping of Precipitation version 7 (GSMaP.G NRT V7, Kubota et al., 2020).

4.2. Model calibration and validation

The MGB hydrological model has several parameters (auxiliary data, dynamic and static variables) that need to be adjusted/

Table 1
IMERG V06 Final run performance indicators compared to the gauges, coefficient of determination (R2), Relative Bias (in %), Probability Of Detection (POD) and False Alarm Rate (FAR). Statistics derived for a threshold of 0.1 mm/h.

Period	R^2	Relative Bias (%)	POD	FAR
2012–2020	0.60	1.77	0.80	0.19
2020	0.58	5.10	0.77	0.13

calibrated in order to properly estimate the discharge for the various unit-catchments locations in the basin. We considered, as a baseline, the model's parameter setup that is adopted operationally through the GSMaP.G NRT V7 product for the Niger basin (https://mgb-hyfaa.pigeo.fr/). This version evolved from the version implemented by Fleischmann et al. (2018) for the Upper Niger River - the drained area of the Niger River upstream Niamey city (focus of interest of this study), which showed considerable ability to characterize the multiple dynamic and hydrodynamic processes of a complex large scale semi-arid wetland soil type, which include infiltration, evapotranspiration, discharges, among others. However, given that the choice of the precipitation product is a critical factor that influences the accuracy of the discharge simulations, by adopting the IMERG.F V06 precipitation product to force the MGB model, additional parameter set-ups/adjustments were required to compensate the bias in IMERG. Two model parameters have a strong influence on the simulated discharges when considering IMERG.F V06 in the place of GSMaP.G NRT V7 (operational version) precipitation product: the maximum soil water storage (Wm, based on ARNO rainfall-runoff model; Todini, 1996) parameter and parameter from the variable contributing area model for runoff generation (b). The model adjustment from GSMAP to IMERG is only marginal because both rainfall products have a lot in common. They are both Level-3 precipitation products based on the Global Precipitation Measurement Mission (GPM) and geostationary constellation databases (microwave and infrared observations).

Given that, in order to better represent the observed discharge distribution over the Niger 'red floods', especially at Niamey for the 2020 hydrological year with the IMERG.F V06 rainfall estimates, a sensitivity analysis with the model parameters was carried out considering the MGB Wm and b parameters, which vary according to each watershed. The set of experiments, illustrated on Fig. 3b, was performed considering different combinations of the aforementioned model parameters (Wm and b). Model performance

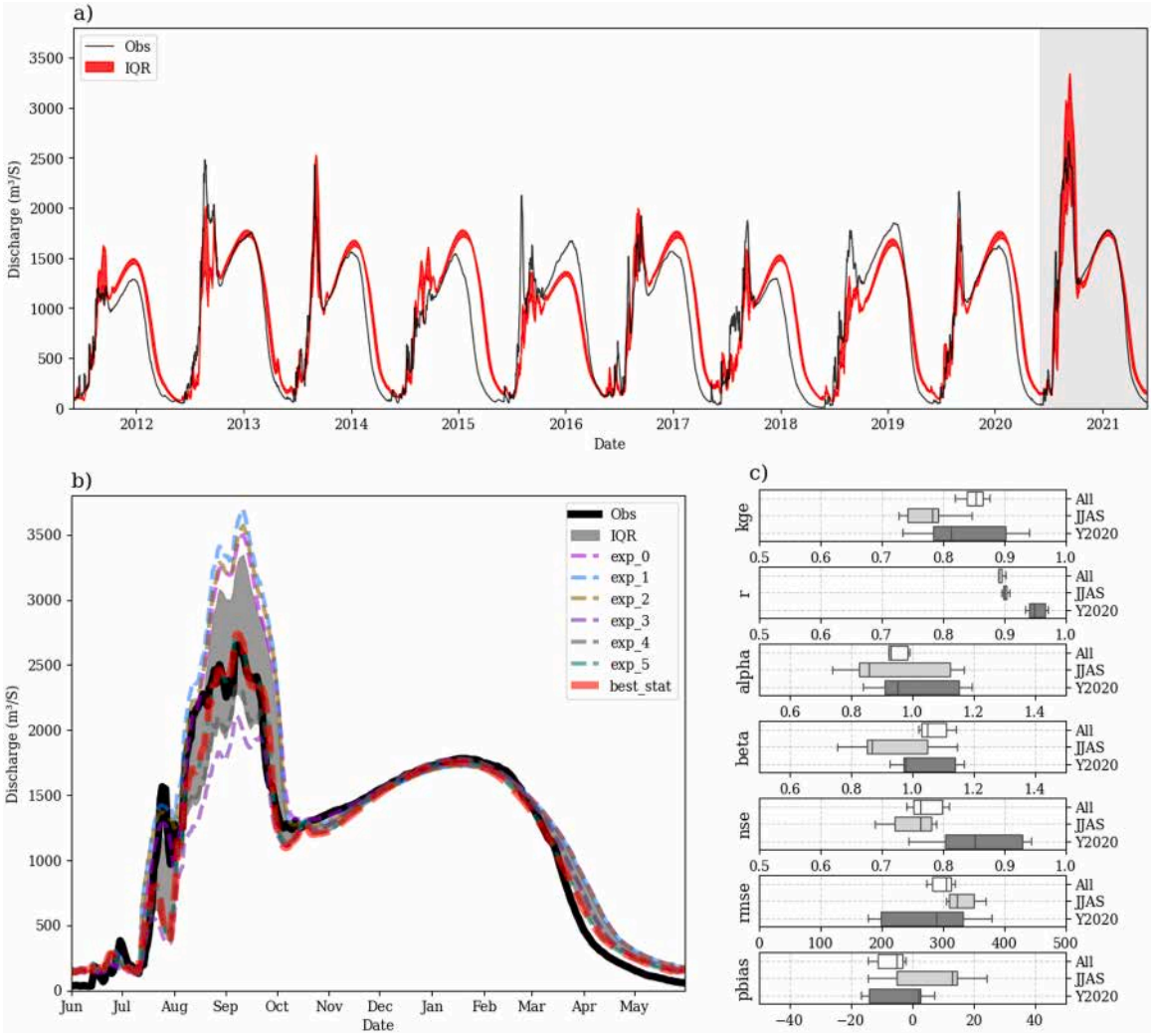

Fig. 3. (a) Observed discharge time series of the Niger River at the Niamey station (black) and discharge simulated (IQR of all experiments) by the MGB model (shaded in red), from 2012 to 2020 hydrological years. (b) The 2020 hydrological year discharges zoom for each experiment (dashed lines), the IQR of all experiments (shaded in gray) and the optimum experiment distribution (red dashed line) compared to the observed discharge (black solid line). (c) Box-plot of overall statistics per sampling period (All: entire distribution from 2012 to 2020, JJAS: all 'red floods' of 2012–2020 period and Y2020: 2020 hydrological year only).

sensitivities were evaluated with the following metrics for daily discharges: Nash-Sutcliffe (NSE, Nash and Sutcliffe, 1970), Kling–Gupta efficiency (KGE, Gupta et al., 2009), Pearson correlation coefficient (r), root-mean-square error (RMSE) and relative bias (pBias). Fig. 3-c depicts the experiment performances per sampling period (All: entire distribution from 2012 to 2020, JJAS: all 'red floods' of 2012–2020 period and Y2020: 2020 hydrological year only). Overall it is notable that the experiments outperform for the Y2020 period, especially in terms of r (ranging from 0.93 to 0.97), followed by the NSE score (from 0.74 to 0.94). On the other hand, the JJAS sampling period has the lowest scores, e.g., KGE of 0.63–0.85 and NSE of 0.69–0.79, with the highest RMSE 300–380 $m^3 . s^{-1}$. This can be explained by the inter-annual effect caused by the different occurrences/amounts of MCS's precipitation during this period over the regions closest to Niamey, being more difficult to be represented by the hydrological model. The best performance statistics results are shown in Table 2. The NSE, KGE and r values obtained, 0.79; 0.78; 0.9 respectively, show a good representation of the 'red flood' (JJAS) discharge distributions over the years. The objective set when adjusting the parameters was a better representation of the 2020 'red flood'. The discharges simulated by the model during the 2020 hydrological year are therefore very close to observations (seen in Fig. 3), with values of 0.94 for NSE and KGE; 0.9 for r and a pBiais of 1.98 %. The model's ability to represent the hydrological years between 2012 and 2020 (study period) is also very satisfying, with NSE, KGE and r values equal to 0.81, 0.87 and 0.9 respectively, and a bias of −3 %.

4.3. Delimitation of the area contributing to the red flood

The domain used for the model (black contour in Fig. 1) represents a surface area of 652777 km^2 subdivided into 4310 unit catchments. In this study we are particularly interested in the red flood, occurring during the rainy season in Niamey and due to rainfall occurring in the vicinity and over Sahelian west-bank tributaries of the Niger, in Burkina Faso. The corresponding area is highlighted in white in Fig. 1. Inside the model, it corresponds to the 20 % of mini-basins that are the closest to Niamey. It includes 585 unit catchments with a total area of 130786 km2. In terms of rainfall forcing it involves 1118 pixels of the original 0.1° IMERG grid.

5. Numerical method to quantify the hydrological impact of MCSs

In this section, we describe how the data and model from the previous sections are combined in order to quantify the impact of individual MCSs on the rise of the discharge simulated in Niamey. The two main satellite databases we use have different spatial resolutions (4 km for Toocan and 10 km for IMERG). For reasons of uniformity of spatio-temporal information, TOOCAN's cloud mask spatial resolution was resampled to match IMERG spatial resolution. The two databases were then merged. This led to the creation of a new MCS-Rain database containing high resolution (30 min – 0.1°) rain maps for each MCS. From this, the contribution of each MCS to the daily rainfall accumulation over the area of origin of the red flood (Fig. 1 – white shading) could be calculated and the suppression of one or several MCSs in the forcing data could be tested through the MGB model. All stages of the methodology are detailed in the following sections.

5.1. Creation of a new MCS-Rain database

5.1.1. TOOCAN-IMERG merging

To create a new database that relates each individual MCS to its associated rainfall, we first merged TOOCAN and IMERG databases. The TOOCAN cloud mask resolution was first changed from 4 km to the IMERG resolution of 10 km. The temporal resolution of 30 min is preserved. Then, segmented images of convective systems and all associated 30-min rain pixels were extracted over the entire period (January 2012 to December 2020) and for the study area. Fig. 4 shows the trajectory of a given MCS and its associated precipitation from IMERG, within the Upper Niger basin. This MCS initiated on August 21, 2020 at 7 pm, enters the Middle Niger Basin (study sub-basin, white zone in Fig. 4) on August 21, 2020 at 7:30 pm, exits the following day, August 22, 2020 at 9:30 am and finally dissipates at 1:30 pm. This precipitating system spent around 75 % of its life cycle over the study sub-basin, mainly during its mature phase.

Fig. 5 schematizes the result of the merging over the area of interest. Each 0.1° resolution pixel from each 30-minute IMERG rain map is associated with the label of the MCS which was covering this pixel at that time according to TOOCAN. IMERG pixels which were not included in an MCS contour are not labelled; they might however have a non-zero rainfall in IMERG product.

5.1.2. Rainfall quantity associated with each MCS over the red flood drainage area

From the MCS-rain database different rain amounts associated with the MCSs can be quantified. For each MCS, the sum of its daily rainfall accumulation on each 0.1° pixel can be calculated over the whole area of interest by summing the 48 maps at 30-minute time step; this represents the contribution of the given MCS to the total daily rainfall from IMERG.

The total amount of rainfall or volume integrated over the sub-basins in space and time while the MCS is crossing the area is also

Table 2
MGB model performance indicators per analysis period, based on the optimum discharge simulation.

Period	NSE	KGE	RMSE	r	pBias
Entire (2011.06–2021.09)	0.81	0.87	273.48	0.9	-3.03
JJAS "red floods" 2011–2021	0.79	0.78	304.98	0.9	12.93
2020 hydrological year	0.94	0.94	178.18	0.97	1.98

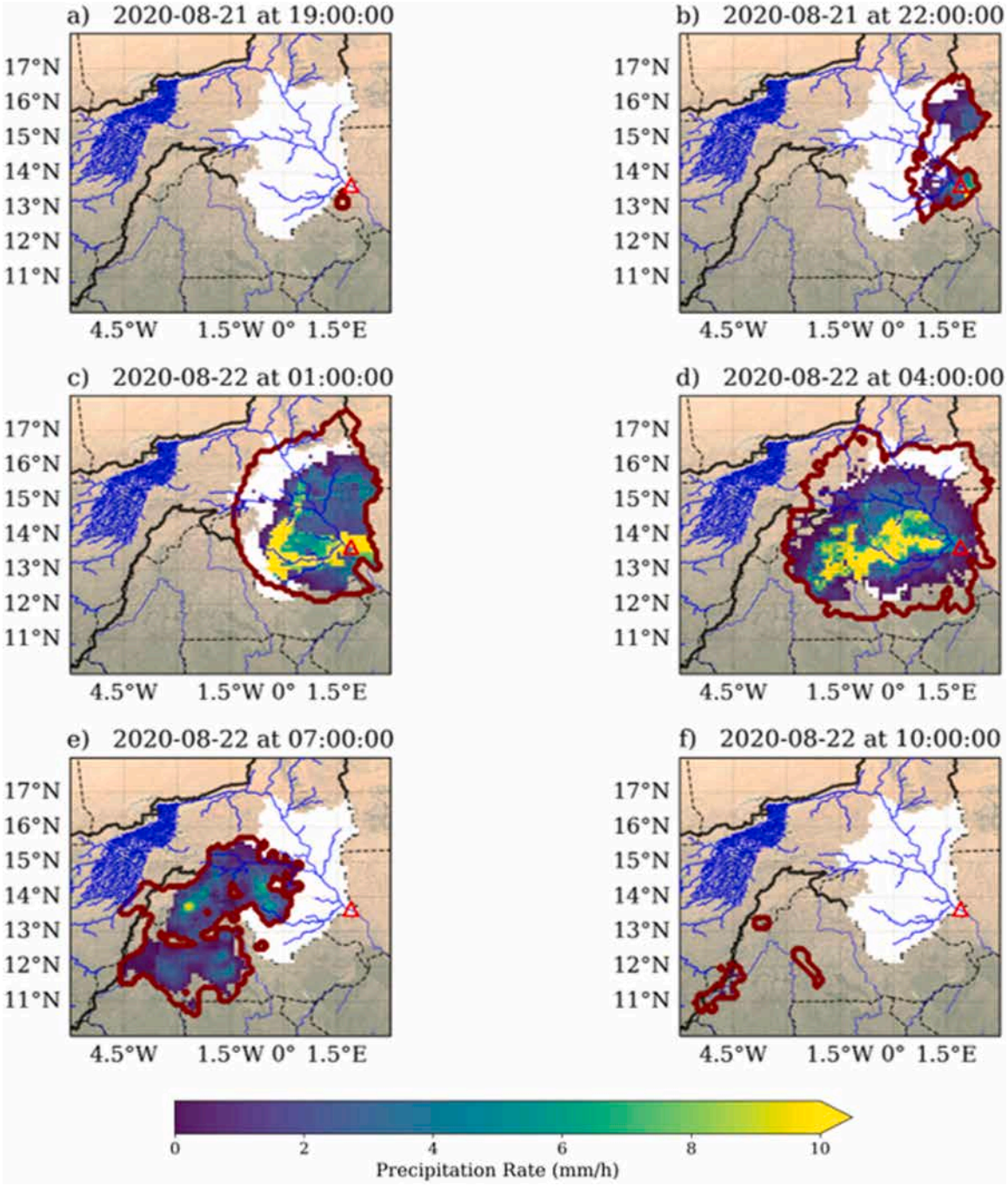

Fig. 4. Red contours: MCS identified on a Meteosat infrared image, using the TOOCAN algorithm, with a brightness temperature (TB) below 235 K. This MCS is tracked over the study sub-basin (white area), between August 21 and 22, 2020. Color map: rainfall (in mm h-1) from IMERG. Different moments in the life cycle of the MCS are represented on the figure: (a) the initiation phase (August 21 at 19:00 UTC); (b, c, d) three moments in the development phase (August 21 at 22:00 UTC, August 22 at 01:00 UTC; 04:00 UTC) and (e, f) two moments when the MCS decays and leaves the study area, in its dissipation phase (August 22 at 07:00 UTC and 10:00 UTC).

quantified.

This is an interesting parameter to understand the hydrological response, as a basin itself acts as a natural space-time 'integrator' of rainfall. Most studies that analyze flooding in the Sahel concentrate on rainfall peak intensity and local extreme values rather than on the space-time integration of the rain produced by a given storm over a basin. For large systems producing stratiform rainfall where intensity is not the determining factor, this parameter appears to be important especially as it derives from the combination of rainfall

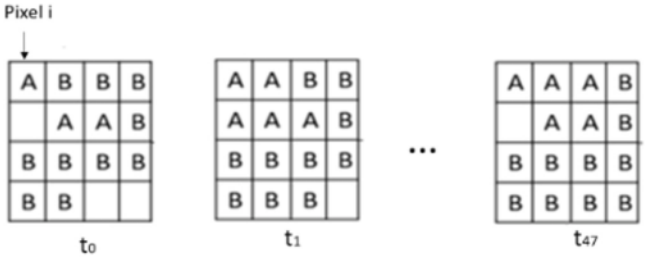

Fig. 5. Illustration of the labelling of the 0°1 pixels with the associated MCS identifier. In this example 2 MCSs, labelled A and B were detected by TOOCAN over the domain during the illustrated 1-day period. A day consists of 48 30-minute time steps (t0; t1; …; t47).

intensity, system size and the time taken for these systems to cross the region (Maranan et al., 2018). The rainfall volume V (in mm. km^2) is a function of the size of the system, its duration and the distribution of the rainfall intensities as the MCS overlap the study sub-basin. It corresponds to the sum over all pixels of the red flood area (1118 pixels in total) of the accumulated rainfall during the duration of the storm over the area. Subsequently, this parameter will be used to identify the most precipitating MCSs.

5.2. Hydrological modeling experiments

The MCS-rain data base is then used to analyze the impact of the MCSs on the simulated discharge at Niamey through numerical experiments. For this purpose, the original rain forcing used for the reference simulation presented in Section 4 (Fig. 3) is modified to simulate different scenarios and exclude one or several MCSs. Fig. 6 illustrates these experiments with an example of rain forcing over the study area, before and after suppression of one MCS.

6. Hydrometeorological revisit of 2020 major flood events in Niamey

Using the database and simulation set up previously introduced, the exceptional character of the rainy season 2020 and the role of MCSs in the extreme floods recorded that year is analyzed, in three steps.

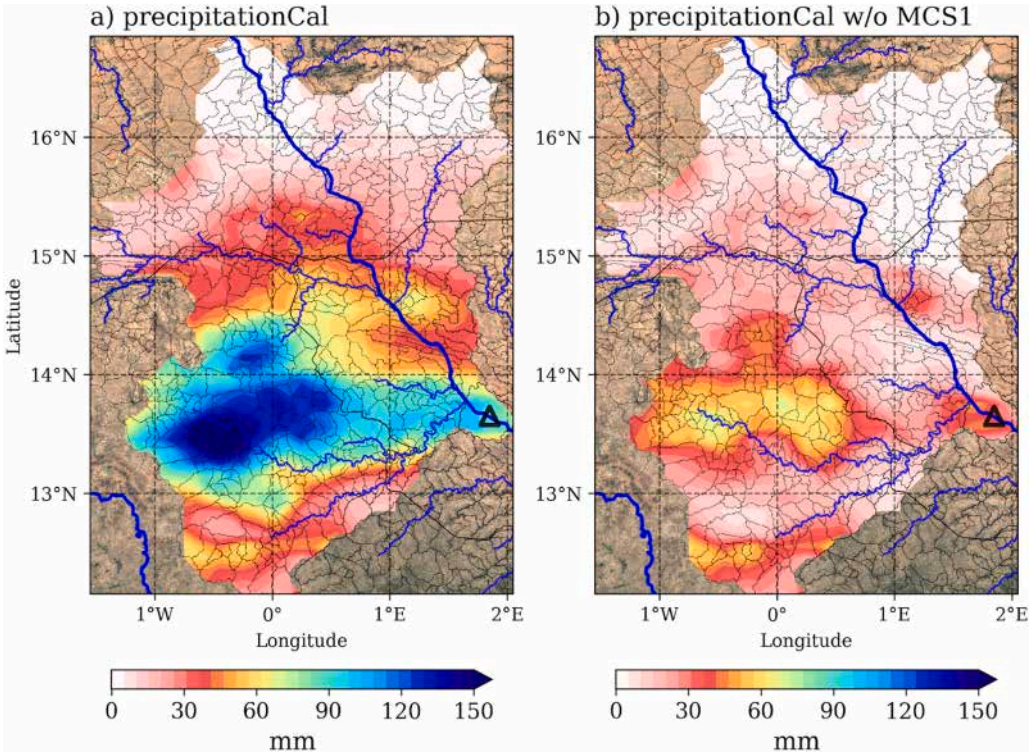

Fig. 6. Illustration of the rain forcing over the area of interest used for hydrological experiments. The contours of the 585 unit-catchments hydrological model grid are shown in black – (a) original rain accumulation based on IMERG. (b) accumulation when one of the MCSs has been excluded. The precipitation accumulation was performed for a time period of 4 days (from 19 to 22 of August 2020).

6.1. Interannual analysis of convective systems and associated rainfall

A total of 9588 rainy systems were observed and tracked over the study area at the 235 K threshold between January 01, 2012 and December 31, 2020. Fig. 7 illustrates their mean monthly (Fig. 7a) and annual (Fig. 7b) occurrence distribution. The monthly distribution shows that most convective systems were observed in the months of June-July-August-September (JJAS), with an average of between 130 and 230 systems per month. The JJAS season corresponds to the monsoon season, and is clearly observed as the preferential period for the occurrence of convective events in accordance with other studies (e.g., Mathon et al., 2002). Fig. 7b, displays the inter annual variability in number (blue bars) and cumulative volume of precipitation associated with MCSs (red curve). Fig. 7b indicates a more homogeneous distribution of the number of systems identified from one year to the next, with a maximum relative deviation of 19 %, while the cumulative annual precipitation by volume (red curve in Fig. 7b) shows greater interannual variability, with a maximum relative deviation of 29 %. It is noteworthy that the year 2020, with the second lowest number of systems observed, has the highest cumulative precipitation. In 2020 the precipitation is 30 % higher than the average total precipitation recorded over the entire study period. This exceptional nature of 2020 was marked by flood events leading to material damage and loss of life, as mentioned in the introduction (Niger Rapport de situation, 2020). Two other years stand out, but less than 2020, for their rainfall accumulations in Fig. 7b, 2012 and 2016, when floods were also reported in Niamey, especially for 2012 which was the first of a series of extreme discharge values recorded in Niamey.

This important result highlights the fact that the number of MCSs in a season is not enough to explain the accumulated rainfall received by the basin, and hence the flood risk. MCSs vary in nature and various environmental factors can influence the size, lifetime and intensity of these systems (Chen et al., 2023) leading to a wide variety in terms of total rainfall production.

To analyze further the exceptional nature of the 2020 rainy season, we present in Fig. 8a, the annual evolution of the precipitation volume as a function of the number of convective systems, for the period 2012–2020. The convective systems were sorted in descending order of precipitation volume – the most rainy system in the first one on the X-axis.

The rise of the cumulative annual rainfall volume can be divided into three distinct stages: i) between the first and 100th most rainy systems a rapid increase is observed; ii) between the 100th and 200th system, the cumulative rainfall stops growing rapidly and iii) beyond the 200th system the increment in rainfall accumulation is insignificant. Each year, the 200 most rainy systems on average represent only 20 % of the total number of convective systems but contribute 90 % of the total annual rainfall volume. The slope is even more marked for 2020 and the zoom on the first 100 systems reveals that the exceptionally strong rainfall accumulation arises from the 10 most rainy systems.

To analyze further, Fig. 8b shows the rainfall volumes associated with each of the 10th most rainy systems for the period 2012–2020. Compared with other years, the distribution of the 10 highest rainfall volumes in 2020 appears uniform. Each system produced a greater volume of rainfall than its corresponding systems in other years; except in 2012 for the systems associated with the first two precipitation volumes. However, the cumulative 10 in 2020 are 22 % higher than in 2012. This is particularly significant given that 2012 was one of the wettest years in the last fifty years, causing severe flooding and loss of life (Sighomnou et al., 2013). We also note that these 10 systems, out of around 1000 identified each year, account for between 20 % (for 2015) and 34 % (in 2020) of the total annual precipitation volume, with an average of 30 % per year.

6.2. Characterization of the ten (10) MCSs associated with the highest rainfall amounts in 2020

The Fig. 9 illustrates the impact over the red flood generation area of the 10 rainiest MCSs over the zone. These 10 systems alone

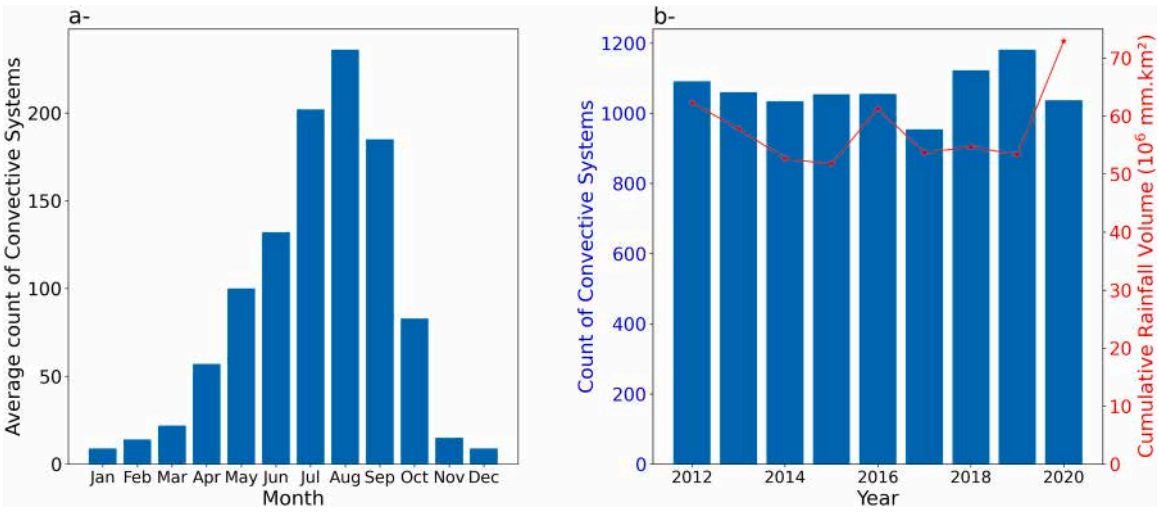

Fig. 7. Histograms of rainfall system distributions in the study area - (a) monthly mean distributions. (b) annual distributions. The red curve in (b), represents the cumulative rainfall volume associated with convective systems each year for the period 2012–2020.

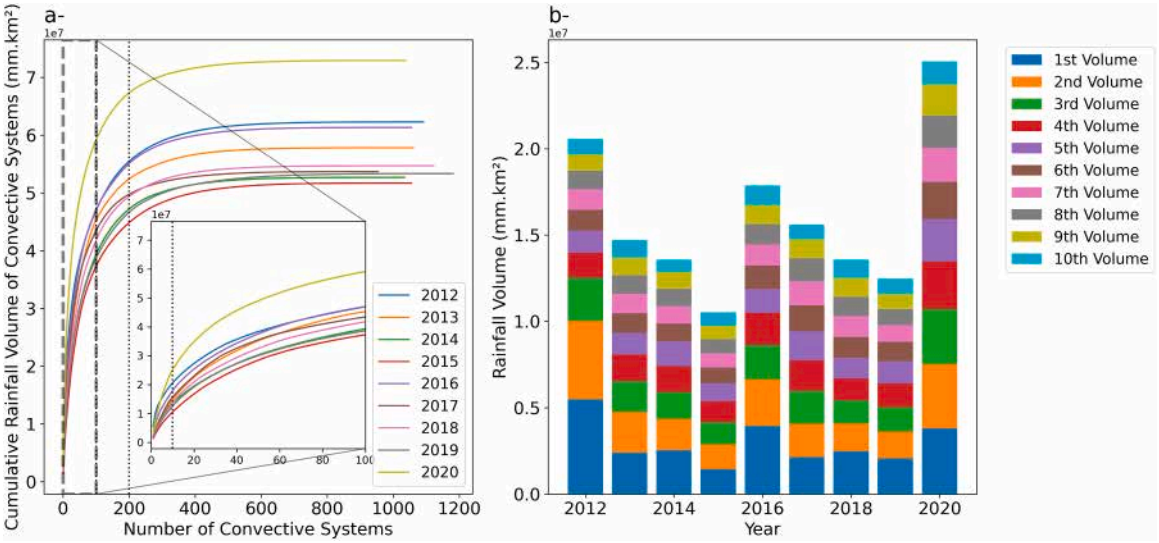

Fig. 8. (a) 9-year cumulative rainfall volume over the study area produced by convective systems as a function of their number (volumes are accumulated from the highest to the lowest volume). (b) bar chart of the 10 largest rainfall volumes produced by the MCSs each year.

explain 20–50 % of the annual rainfall in 2020 over the basin of the 3 tributaries of the Niger, ahead of Niamey.

The characteristics of these 10 rainy systems are compared with the other systems identified in the same year in Fig. 10. These MCSs were identified in the JJAS season, including 5 in August, the peak of the rainy season. Hereafter, we'll refer to all 10 MCSs as "MCS-10".

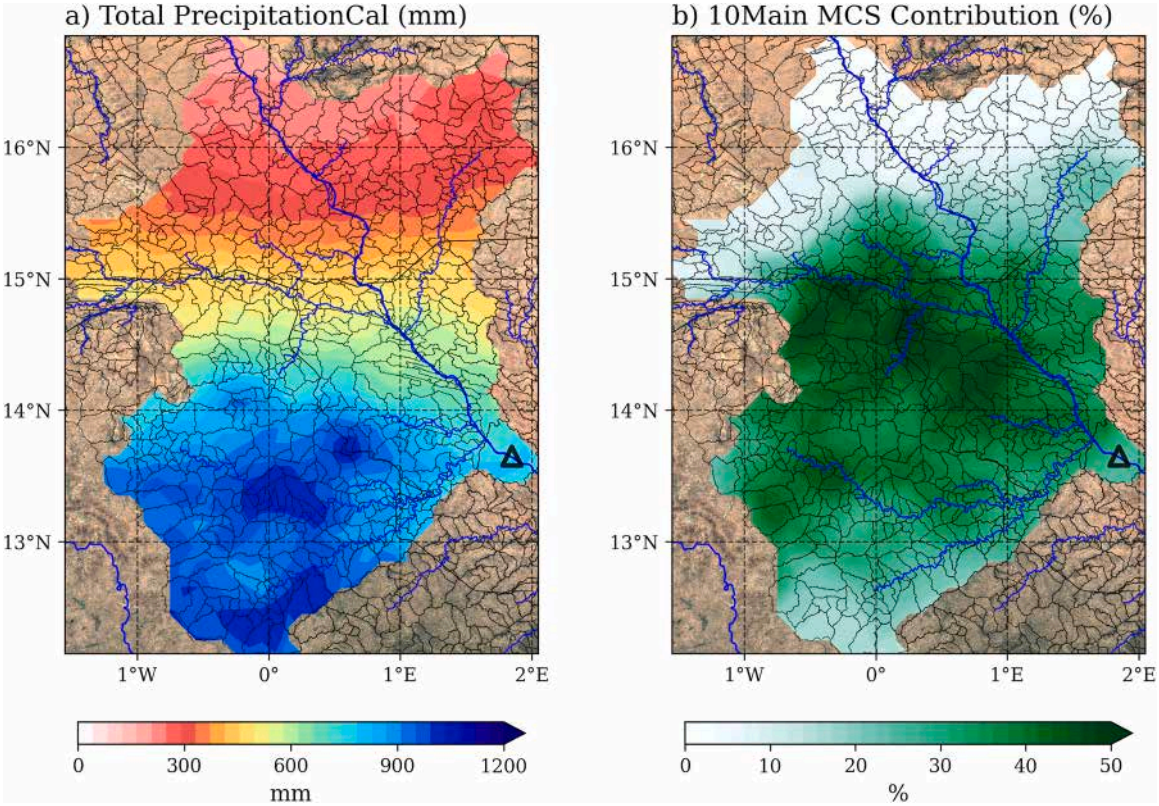

Fig. 9. The JJASO rainy season - (a) Total precipitation (in mm); (b) precipitation contribution (in %) from the 10 main MCSs, over the study area. The black triangles indicate the location of Niamey, the river network and the unit catchment limits are overlayed as blue and black lines, respectively.

Fig. 10a shows the distribution of lifetimes of all the systems identified in 2020 in relation to the maximum rainfall (Pmax at one pixel) they produced. The color coding of the dots indicates the maximum size reached by the systems during their life cycle. We note that 88 % of the convective systems identified in 2020 produced a maximum rainfall less than 20 h^{-1}. MCS-10, represented on the figure by larger dots, are among the 12 % that generated heavy rainfall associated with peaks ranging from 29 to 60 h^{-1}. Their maximum sizes are in the upper tail of the distribution, above the 90th quantile. Eight of the ten MCSs reached sizes greater than 100,000 km^2. These MCS-10 have a relatively long-life cycle, with lifetimes of between 14 and 30 h, and they are among the minority (5 %) that have spent more than 10 h on the study domain (Fig. 10b). Fig. 10b shows the distribution of minimum brightness temperatures as a function of average propagation velocities and system durations in the study area. MCS-10 are cold MCSs, with minimum temperatures ranging from 178 K to 186 K, suggesting strong convective activity within them. Six of these MCS-10 are slow-moving over the study area, with velocities ranging from 5.5 to 8.5 m s-1, while the other four MCSs are moving at velocities exceeding 10 m/s, from 11 to 15 m s-1. These relatively slow or moderate propagation velocities could explain the long hours within the study area. These results are in agreement with previous studies noting the key role of large (Mathon et al., 2002), cold (Taylor et al., 2017; Klein et al., 2018) and long-lived (Feng et al., 2018; Roca and Fiolleau, 2020) MCSs in the tropical extreme rainfall pattern and in flood events. In the East Asian region influenced by the monsoon regime, Ding et al. (2024) noted that reported floods were induced by MCSs with high rainfall volumes and characterized by long lifetimes and higher rainfall rates.

The evolution of the main physical properties of MCSs and associated rainfall as they crossed the study area is further described in Appendix 1 (figure A1). All MCS-10 showed their maximum convective activity (i.e., development phase) over the study area, resulting in high precipitation rates.

6.3. *Impact of MCSs on the record red flood in 2020*

To quantify the hydrological impact of the MCSs a numerical experiment is carried out with the hydrological model presented in Section 4. The reference simulation is the one presented in Fig. 3 based on the IMERG product. Using the MCS-rain database introduced in Section 5, the rain forcing of the model is modified by subtracting the rainfall associated to the MCSs.

First the global impact of all the MCSs (1037) that crossed the 'red flood genesis area' in 2020 is illustrated in Fig. 11. Fig. 11a displays the time evolution of the mean daily rainfall over the study area during the rainy season. Fig. 11b shows the reference simulation (black) and the discharge simulated when all the MCSs from the area have been suppressed (red). As discussed in Section 4, the reference simulation reproduces well the red flood phenomena with the rapid rise of the discharge following the rainy events. When the MCSs are not included in the forcing, the red flood disappears entirely. This is consistent with the previous studies (Casseé et al., 2015, 2016) which have highlighted the role of the convective systems crossing the right bank Niger tributaries on the red flood genesis.

The horizontal dotted line in Fig. 11b shows the value of the critical flood threshold of 1700 $m^3 . s^{-1}$, defined by the Niger Basin Authority. This threshold is exceeded significantly between August and September, the core of the rainy season. This risk of overflow entirely disappears once all the rainfall generated by the convective systems identified during the JJAS season has been eliminated (red curve in Fig. 11b). Simulated discharges decrease considerably, with the peak falling from 2741 $m^3 . s^{-1}$ to 713 $m^3 . s^{-1}$, a drop of 74 %. The simulated mean seasonal flow, between June and September, also falls from 1180 $m^3 . s^{-1}$ to 317 $m^3 . s^{-1}$, a decrease of 73 %.

Next, we assess the individual impact of the 10 rainiest systems. Their contribution to the daily rainfall over the domain is illustrated in Fig. 12a (color bars).

On average, each of these MCSs contributed to 69 % of the daily rainfall on the days when they occurred. In Fig. 12b the discharge

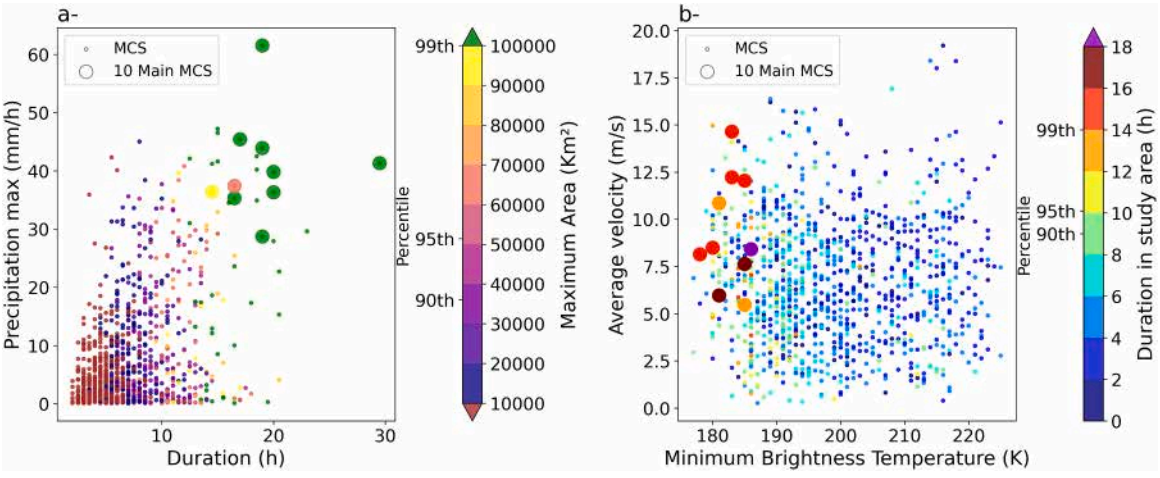

Fig. 10. Scatterplots of - (a) MCSs lifetime as a function of maximum rainfall within them, the color indicates for each MCS, the maximum size reached. (b) Minimum brightness temperature as a function of average propagation speed; colors indicate lifetime in the study sub-basin.

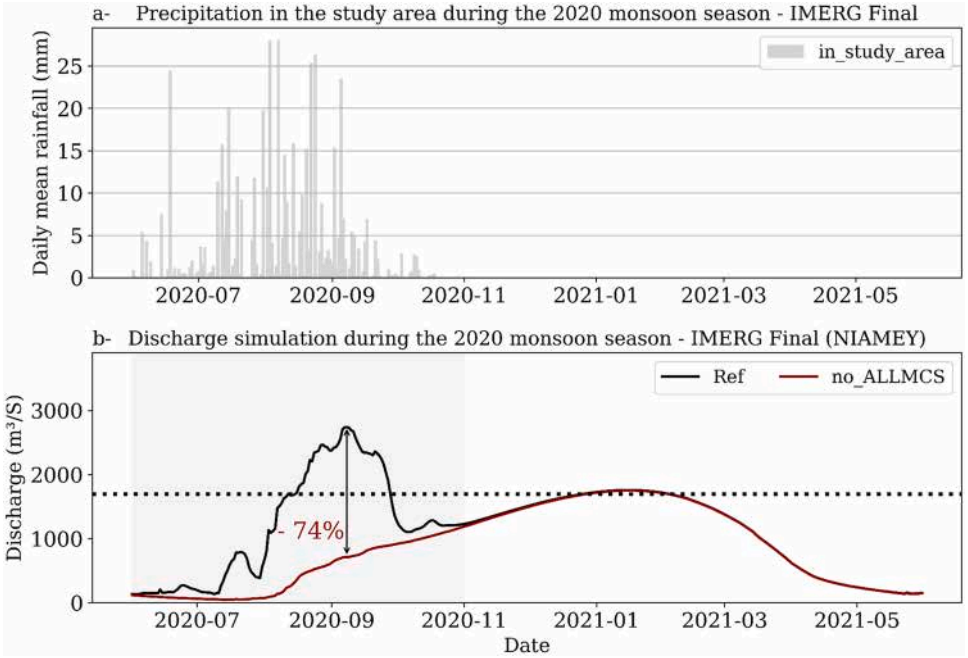

Fig. 11. (a) Time series of mean daily rainfall recorded each day over the study area during the 2020 rainy season. (b) Simulated hydrograph of the River Niger at Niamey during the 2020 hydrological year. The black curve represents the reference simulation and the red curve the simulated discharges after suppression of the rainfall produced by convective systems. The value "-74 %" on the graph indicates the percentage drop in peak discharge. The shading indicates the period of occurrence of the red flood.

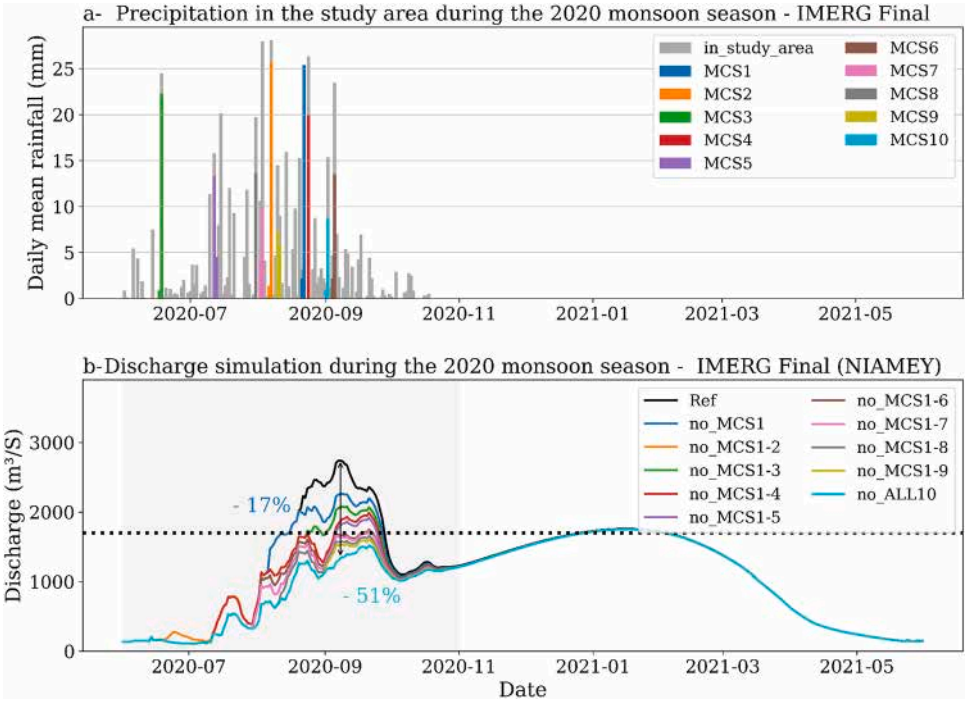

Fig. 12. (a) Time series of mean daily rainfall over the study area (grey) and contribution of each major MCS (colors). (b) Simulated hydrographs for the different forcing experiments. In black the reference simulation with IMERG product. In color, the discharge simulated after successive suppression of each MCS, starting with the one with most rain volume (no_MCS1), then the 2 most rainy (no_MCS1–2), until suppression of the 10 most rainy ((no_ALL10). See also text.

obtained when suppressing each ten MCSs, one at a time, is shown. Compared with the reference simulation (black curve), the simulated flow curve after elimination of all 10 MCSs (cyan curve), is below the critical flood threshold (dotted line). The simulated peak flow decreases from 2741 $m^3 . s^{-1}$ to 1336 $m^3 . s^{-1}$, a diminishing of 51 % (Fig. 12b). The simulated mean seasonal flow between June and September also decreases, from 1180 $m^3 . s\text{-}^1$ to 668 $m^3 . s\text{-}^1$, a drop of 43 %.

The impact of the rainiest MCS (MCS-1) alone is also striking. This MCS, was observed between August 21 and 22, 2020, lasted 19 h over the area, with a precipitation peak of 61.5 mm h-1. The daily rainfall produced by this MCS (blue bars in Fig. 12a), represents 64 % of the rainfall recorded over the study area on August 21 and 98 % on August 22. The flood risk is still present without this MCS, with flow values above the critical flood threshold, but the peak discharge is reduced by 17 % (Fig. 12b) and the mean seasonal flow by 9 %. As discussed in appendix 2, these results on the relative impact of major MCSs are robust to uncertainties in the satellite data and model parameters.

Finally, the dynamics of the discharge increment associated with each of the 10 major MCSs is further analyzed in Fig. 13 concentrating only on the red flood period. Fig. 13b shows the difference in the discharges simulated by the successive experiments displayed in Fig. 12, quantifying the impact on the simulation of each MCS.

Large individual and intense MCSs like the 2 most rainy (MCS1 and MCS2 in Fig. 12 and Fig. 13) can produce an increase in peak discharge of about 500 $m^3 . s\text{-}^1$. The calculations show that these 2 major MCSs alone represent 25 % of the accumulated discharge during the red flood (when all MCSs are considered). Such an increment can lead to a critical level of discharge and serious flooding. Because of their overall size and duration, the MCS with the most volume have also a long-lasting effect on the response, up to several weeks. The delay between the onset of the MCS in the area and the associated peak in discharge can be a few days. These figures show that the inclusion of the proposed method into operational tools could be interesting in terms of prevention and crisis anticipation.

7. Conclusion and perspectives

A method is proposed to highlight the impact of tropical convection on floods, by analyzing the intersection between the trajectory of individual storms and the area within the basin where runoff occurs. The method combines in an original manner existing tools: satellite data for tracking individual convective systems and quantifying the amount of rain they contribute over the basin, and a hydrological model to simulate the discharge. The contribution of individual MCSs on the rise of the Niger river's discharge in Niamey could be quantified, confirming the role of regional convection on the red flood phenomena (Casse and Gosset, 2015). The tool allows a useful visualization of the role of each MCS on the final shape of the hydrograph.

The outputs of the MCSs tracking algorithm, TOOCAN and the IMERG satellite rainfall estimation product were used to create a database of daily rainfall within each individual MCS identified on the study sub-basin over the period 2012–2020. Using the semi-distributed hydrological model MGB, forced with daily satellite rainfall estimation data, the discharge of the River Niger was simulated. In addition, two simulation cases were run to assess the contributions of individual MCSs on the 2020 red flood. Thanks to the flexible database, these simulations were carried out by easily removing the daily rainfall produced by the individual MCSs from the model's forcing data. The method enabled us to quantify the contribution of MCSs to the intensification of the red flood. The main conclusions are presented below:

- The MGB model successfully represents the 2020 red flood. Simulated flows are relatively close to in-situ observations.
- The 2020 red flood disappears completely when the rainfall produced by all the convective systems identified in the sub-basin is removed. These systems contribute 74 % of the simulated peak discharge during the monsoon season and are therefore the main factor in inducing red flooding.
- 10 MCSs associated with the highest rainfall accumulation in 2020, account for 34 % of the total annual rainfall and 36 % of the total rainfall recorded during the rainy season. Their contribution to the peak discharge of the River Niger at Niamey during the 2020 red flood is estimated at 51 %. The rise in discharge due to these MCSs is greater (in percentage terms) than the equivalent rainfall; the hydrological response of a basin being a non-linear process. These 10 MCSs were responsible for the river overflow and therefore for the flooding episodes recorded during the 2020 red flood. The local MCSs are the main factor in the intensification of the red flood. The contribution of a single MCS (the first largest volume of rainfall) to peak discharge is estimated at 17 %.

- 2 major MCSs - the most rainy - alone account for 25 % of the discharge accumulated during the red flood, with an increase in peak flow of around 500 $m^3 . s\text{-}^1$. Such an increment in peak discharge can generate a critical level of discharge and serious flooding. The delay between the arrival of the MCS on the basin and the peak of the hydrological response is typically a few days (5–10 days) which could be interesting for warning.
- The high rainfall accumulation generated by these MCSs, which have led to river overflows, are the result of a combination of several characteristics of the life cycle of these MCSs, such as their large size, the intensity of convective activity, their relatively slow propagation velocities and their long lifetimes in the basin. Monitoring these MCSs parameters could be useful information to provide to relevant authorities in complement to other indicators of flood risk.

The findings of this study open up the possibility of forecasting flows on a catchment scale and anticipating flood events, through a good representation of MCSs at the origin of extreme rainfall events. Nowadays, several studies (e.g. Feng et al., 2023; Prein et al., 2024) have focused on improving our understanding and ability to represent MCSs within meteorological models, though there is still room for improvement (Vogel et al., 2021). MCSs predictions from these meteorological models or statistical predictions, combined with precipitation outputs, could be used as forcing for hydrological models and thus contribute to the improvement of flood

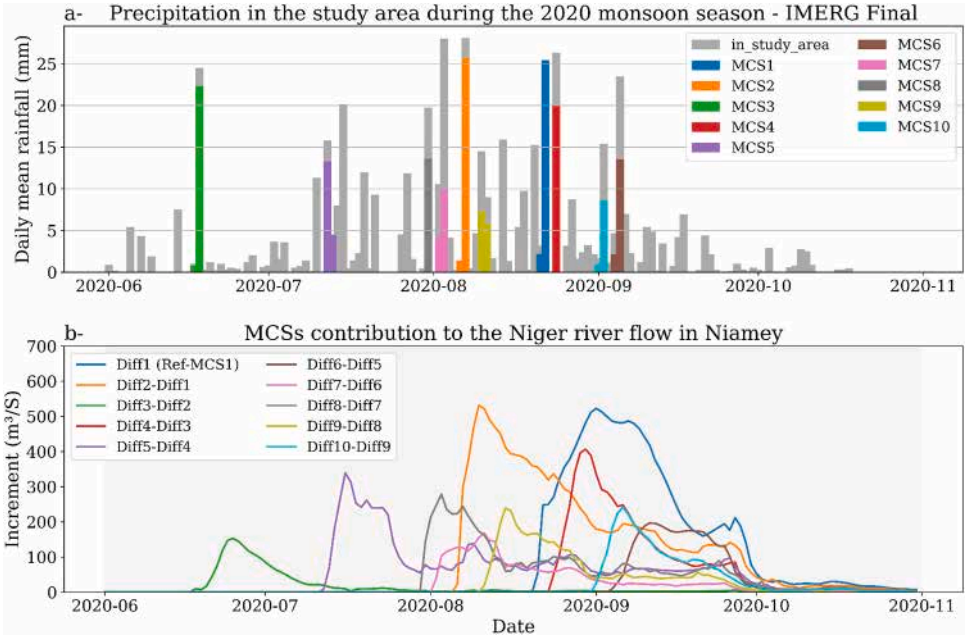

Fig. 13. derived from Fig. 12. (a) Time series of mean daily rainfall over the study area (grey) and contribution of each major MCS (colors). (b) Contribution to the simulated discharge (m3/s) of each individual MCS (the color code is the same as in a).

forecasting and early warning systems. Likewise, near-real-time precipitation datasets and MCSs tracking can be very useful for hydrometeorological monitoring at catchment scale. This study, using MCSs parameters and adapted to hydrological monitoring, provides a new perspective for examining and quantifying the impact of MCSs intensification on flood risk in tropical watersheds, in the context of global warming.

The method could be transferred to analyze flood risk in other regions. Recent floods in southern Brazil between April and May 2024, affected around 1.9 million people (Brésil: Inondations dans le Rio Grande do Sul, IFRC WWW Document, 2024). The rainfall recorded during these floods was intense and two to three times higher than the May average for the region (Paris, n.d.). In this case, the use of satellite measurements, for example, has become essential both for characterizing the atmospheric environment (Reboita et al., 2024), which favoured the occurrence of the associated extreme rainfall episodes, and for understanding the flood dynamics (Laipelt et al., 2025).

CRediT authorship contribution statement

Thomas Fiolleau: Writing – review & editing, Methodology, Formal analysis. **Eric-Pascal Zahiri:** Investigation, Formal analysis, Conceptualization. **Modeste Kacou:** Investigation, Formal analysis, Conceptualization. **Marielle Gosset:** Writing – review & editing, Methodology, Investigation, Funding acquisition, Formal analysis, Conceptualization. **Oliveira Rômulo:** Writing – review & editing, Methodology, Investigation, Formal analysis, Data curation, Conceptualization. **Fatou Josiane Guehi:** Writing – review & editing, Writing – original draft, Methodology, Investigation, Formal analysis, Data curation, Conceptualization.

Declaration of Competing Interest

The authors declare that they have no known competing financial interests or personal relationships that could have appeared to influence the work reported in this paper.

Acknowledgements

The authors wish to thank the ESPRI/IPSL data center and Remy Roca for providing MCSs data. The TOOCAN data are available from **http://toocan.ipsl.fr** with the DOI https://doi.org/10.14768/1be7fd53-8b81-416e-90d5-002b36b30cf8. We also wish to thank the Autorité du Bassin du Niger (ABN) for their collaboration.

Financial support: Fatou Josiane Guehi and Dr Romulo Jucá Oliveira were partly funded by the AFD/IRD CECC project

Appendix 1. Evolution of the characteristics of the MCSs over the study domain and during their life cycle

To understand how the high productivity of these MCSs is built up throughout their life cycle, Fig. A1 shows the evolution of the key

parameters of size, minimum brightness temperature and maximum precipitation associated with each MCS-10. As expected, most of the precipitation occurs during the growth phase of the systems. For each of these MCSs, convective activity and size both reach their peak inside the study area. The precipitation maximum is preceded by a minimum in brightness temperature, indicating the peak in vertical cloud development, and is followed by a maximum in horizontal cloud development, reflected by a peak in size. This is consistent with several studies of MCSs climatology, including those by Goyens et al. (2012) in the Sahel and Chen et al. (2020) in China.

The capacity of these MCSs to produce high rainfall volumes is not developed in the same way. In fact, MCS4, MCS9 and MCS10, although less extensive than the other MCSs in the group of ten, have a life cycle marked by a succession of rainfall peaks typical of multicellular thunderstorms. The convective activity of these multiple cells, combined with the long life of the systems, could explain the high rainfall accumulations observed. The convective activity of MCS1, MCS2 and MCS5 is characterized by a single intense rainfall peak. These systems reach larger sizes than those observed in the other systems of the Group of 10 during their life cycle. The significant cumulative rainfall of these MCSs is therefore be related to a combination of size, peak precipitation intensity and long lifespan. Finally, MCS3, MCS6, MCS7 and MCS8 are characterized by a large peak, indicating long-lasting thunderstorm activity over the study area. This long-lasting thunderstorm activity, with a peak above 25 mm/h for at least 3.5 h and 5.5 h at most, combined with the size of the systems, explains the high total rainfall observed.

This indicates that the MCSs associated with the 10 highest rainfall volumes have specific characteristics regarding the formation of their significant cumulative rainfall in the study area. These results suggest that, on a catchment scale, the capacity of MCSs to produce high rainfall volumes is not developed in the same way. The size, intensity of convective activity, lifetime and propagation velocity of these systems would therefore be key factors to consider for MCSs forecasting in meteorological models, an area of considerable research interest (e.g. Prein et al., 2020), especially for MCSs generating significant rainfall amounts over a catchment.

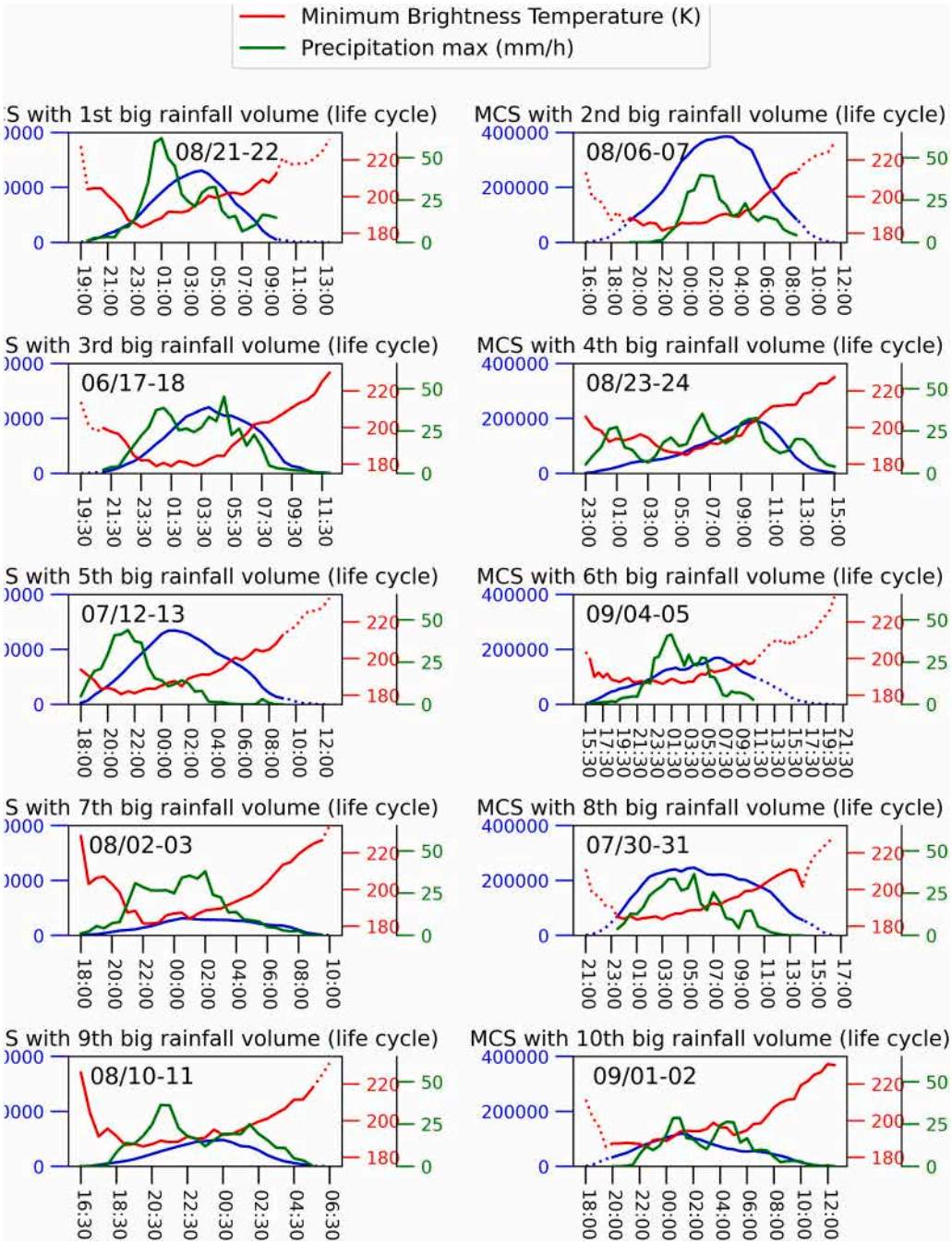

Fig. A1. Evolution of size, minimum brightness temperature and maximum rainfall for each MCS in the MCS-10 group over their life cycle. The part of the curves in solid lines indicates the time at which the MCSs are observed in the study sub-basin. The inscriptions inside each panel represent the dates of occurrence of these MCSs in month/days format

Appendix 2. Sensitivity of the results to uncertainties in the satellite data and hydrological modeling

As discussed in Sections 3 and 4, the individual components of our novel chain of analysis carry some uncertainties.

For the first component, the TOOCAN product for MCS tracking, the various sources of uncertainties have been discussed in Fiolleau and Roca (2013); (2024). They can originate from the algorithm itself or/and from the impact of radiometric errors and missing geostationary images. Unlike classical two-step, overlap-based tracking algorithms that rely on independent image matching and are prone to artificial splitting and merging artifacts, TOOCAN performs detection and tracking simultaneously within one spatio-temporal framework, guaranteeing physical continuity and a coherent system life cycle while fully suppressing split and merge

artifacts. Statistics from Fiolleau and Roca (2013) show that TOOCAN is able to detect and time correctly MCS with maximum areas as small as 100 km2. Regarding the harmonization of the IR geostationary dataset, Fiolleau et al. (2020) calibrated the Meteosat observations using the SCARAB instrument onboard Megha-Tropiques as an absolute reference, achieving a 0 K mean bias and a 1.5 K residual uncertainty across the tropical belt. The robustness of this calibration was subsequently evaluated in Fiolleau and Roca (2024) through a series of 134 independent sensitivity runs, in which random Gaussian noise ($\sigma = 1.5$ K) was added to the infrared brightness temperatures to simulate the effect of radiometric uncertainty. This ensemble-based perturbation experiment was used to assess how such uncertainties might propagate through the TOOCAN segmentation process. The results demonstrated a high stability of the algorithm: the relative confidence intervals in Deep Convective System occurrence were found to be ≈ 0.5 % for short-lived systems (<5 h) and ≈ 1.4 % for long-lived systems (>20 h). These findings confirm that the 1.5 K residual radiometric uncertainty in the calibrated infrared data has a negligible impact on both the detection and the lifecycle statistics of convective systems. Another source of uncertainty lies in the number of consecutive missing infrared images used for tracking. Because TOOCAN relies on continuous 30-minute geostationary observations to reconstruct the full three-dimensional evolution of convective systems, any interruption in the image sequence can affect tracking continuity and, consequently, the accuracy of system lifetimes and occurrence statistics. Fiolleau and Roca (2024) showed that while the algorithm is highly tolerant to short gaps (≤2 h), longer gaps, particularly beyond three consecutive hours, can lead to artificial prolongation of systems and overestimation of long-lived DCS occurrences. However, given the very low number of missing METEOSAT images during the analysis period (availability > 99.9 %), this uncertainty can be considered negligible for the results of this paper. Overall, these three sources of uncertainty, algorithmic, sensitivity, radiometric calibration, and data continuity have been rigorously quantified in previous TOOCAN evaluations. Their combined effect is negligible compared to the uncertainties in the two other components of the chain, the Imerg rainfall product and the hydrological model.

The second component is the rainfall estimation from IMERG V06 product. As discussed in Section 3.2 and reported in Table 1, the IMERG V06 final run product used in this study was compared to a rain gauge network situated near Niamey. In 2020, the product exhibits a bias of 5 % (higher than the average bias over the 2012–2020 period). This value was taken as a reference to carry out an uncertainty propagation analysis through our chain of analysis. As in Section 6.3, the hydrological model is run while the rainfall associated with the major MCS is removed from the rain input. However, this time, 2 additional experiments are carried out, with a positive (+ 5 %) and a negative bias (-5 %) on the MCS rainfall. The results are illustrated in Figure A2 (a) and reported in Table A2.

The impact of the rainfall bias is almost negligible. The relative impact of the MCS varies only marginally (by about 1 %).

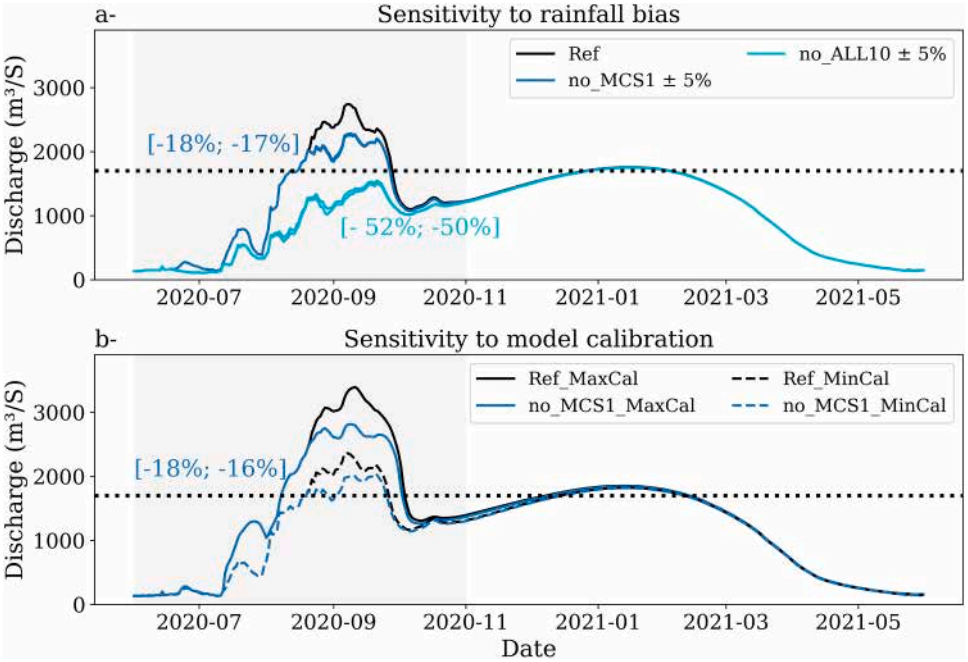

Fig. A2. Discharge sensitivity to: (a) an additive factor of ±5 % bias on MCSs rainfall input; (b) two extreme model calibration setups (MaxCal and MinCal)

Table A2
contribution of the rainiest (MCS1) and 10 rainiest (MCS-10) MCSs, to the simulated discharge (in %), for different sensitivity tests. Left column, reference simulation (as in Section 6.3, Fig. 12), other columns, numerical experiment as indicated

	Best Cal (reference)	Model parameters Min Cal	Model parameters Max Cal	Bias on rain (+5 %)	Bias on rain (-5 %)
MCS1 impact on discharge	17 %	16 %	17.6 %	17.8 %	16.8 %
MCS-10 impact on discharge	51 %	47 %	52 %	52 %	50 %

The third component of the chain is the hydrological model. The sensitivity of the model to its parameters is discussed in Section 4.2

and illustrated in Fig. 3. For the reference run, the model's parameters were chosen to best represent the season 2020. However, multiple runs were made, with a range of acceptable values for the 2 main parameters *Wm* and *b*, as shown by the gray shading in Fig. 3 which illustrates model uncertainty. To check the sensitivity of our result to this uncertainty we carried out additional experiments where the impact of MCS was analyzed for several model setups. The results are illustrated in Figure A2 (b) and Table A, for the model set up corresponding to the interquantile spread (in Fig. 3); one model setup (labeled as MinCal in Fig. and Table A2) leads to a strong underestimation of the discharge, while the other (MaxCal) produces on the contrary a high discharge.

While the absolute values of discharge are different, the relative impact of the MCSs stays stable as reported in Table A2, and the conclusions of our work are robust to the considered uncertainties.

Data availability

Data will be made available on request and with the agreement of the owners.

References

ABN, 2021. Note Technique Sur Les Previsions De Tendance De La Crue Guineenne 2020/2021.

Alfieri, L., Bisselink, B., Dottori, F., Naumann, G., de Roo, A., Salamon, P., Wyser, K., Feyen, L., 2017. Global projections of river flood risk in a warmer world. Earths Future 5, 171–182.

Aryee, J.N.A., Afrifa, F.O.T., Agyapong, K.-H., Gyau Frimpong, N.A., Quagraine, K.T., Davies, P., 2024. Quantifying climatic heavy-precipitation-induced floods in West Africa using multiple precipitation indices. Sci. Afr. 25, e02309. https://doi.org/10.1016/j.sciaf.2024.e02309.

Atiah, W.A., Amekudzi, L.K., Danuor, S.K., 2023. Mesoscale convective systems and contributions to flood cases in Southern West Africa (SWA): a systematic review. Weather Clim. Extrem 39, 100551. https://doi.org/10.1016/j.wace.2023.100551.

Bao, J., Stevens, B., Kluft, L., Muller, C., 2024. Intensification of daily tropical precipitation extremes from more organized convection. Sci. Adv. 10, eadj6801. https://doi.org/10.1126/sciadv.adj6801.

Biasutti, M., 2019. Rainfall trends in the African Sahel: Characteristics, processes, and causes. WIREs Clim. Change 10, e591. https://doi.org/10.1002/wcc.591.

Brésil: Inondations dans le Rio Grande do Sul | IFRC [WWW Document], 2024. URL https://www.ifrc.org/fr/emergency/brazil-rio-grande-do-sul-floods (accessed 7.4.24).

Calvin, K., Dasgupta, D., Krinner, G., Mukherji, A., Thorne, P.W., Trisos, C., Romero, J., Aldunce, P., Barrett, K., Blanco, G., Cheung, W.W.L., Connors, S., Denton, F., Diongue-Niang, A., Dodman, D., Garschagen, M., Geden, O., Hayward, B., Jones, C., Jotzo, F., Krug, T., Lasco, R., Lee, Y.-Y., Masson-Delmotte, V., Meinshausen, M., Mintenbeck, K., Mokssit, A., Otto, F.E.L., Pathak, M., Pirani, A., Poloczanska, E., Pörtner, H.-O., Revi, A., Roberts, D.C., Roy, J., Ruane, A.C., Skea, J., Shukla, P.R., Slade, R., Slangen, A., Sokona, Y., Sörensson, A.A., Tignor, M., van Vuuren, D., Wei, Y.-M., Winkler, H., Zhai, P., Zommers, Z., Hourcade, J.-C., Johnson, F.X., Pachauri, S., Simpson, N.P., Singh, C., Thomas, A., Totin, E., Arias, P., Bustamante, M., Elgizouli, I., Flato, G., Howden, M., Méndez-Vallejo, C., Pereira, J.J., Pichs-Madruga, R., Rose, S.K., Saheb, Y., Sánchez Rodríguez, R., Ürge-Vorsatz, D., Xiao, C., Yassaa, N., Alegría, A., Armour, K., Bednar-Friedl, B., Blok, K., Cissé, G., Dentener, F., Eriksen, S., Fischer, E., Garner, G., Guivarch, C., Haasnoot, M., Hansen, G., Hauser, M., Hawkins, E., Hermans, T., Kopp, R., Leprince-Ringuet, N., Lewis, J., Ley, D., Ludden, C., Niamir, L., Nicholls, Z., Some, S., Szopa, S., Trewin, B., van der Wijst, K.-I., Winter, G., Witting, M., Birt, A., Ha, M., Romero, J., Kim, J., Haites, E.F., Jung, Y., Stavins, R., Birt, A., Ha, M., Orendain, D.J.A., Ignon, L., Park, S., Park, Y., Reisinger, A., Cammaramo, D., Fischlin, A., Fuglestvedt, J.S., Hansen, G., Ludden, C., Masson-Delmotte, V., Matthews, J.B.R., Mintenbeck, K., Pirani, A., Poloczanska, E., Leprince-Ringuet, N., Péan, C., 2023. IPCC, 2023: Climate Change 2023: Synthesis Report. Contribution of Working Groups I, II and III to the Sixth Assessment Report of the Intergovernmental Panel on Climate Change [Core Writing Team, H. Lee and J. Romero (eds.)]. IPCC, Geneva, Switzerland. Intergovernmental Panel on Climate Change (IPCC). https://doi.org/10.59327/IPCC/AR6-9789291691647.

Casse, C., Gosset, M., 2015. Analysis of hydrological changes and flood increase in Niamey based on the PERSIANN-CDR satellite rainfall estimate and hydrological simulations over the 1983–2013 period. Proc. IAHS 370, 117–123. https://doi.org/10.5194/piahs-370-117-2015.

Casse, C., Gosset, M., Peugeot, C., Pedinotti, V., Boone, A., Tanimoun, B.A., Decharme, B., 2015. Potential of satellite rainfall products to predict Niger River flood events in Niamey. Atmos. Res 163. https://doi.org/10.1016/j.atmosres.2015.01.010.

Casse, C., Gosset, M., Vischel, T., Quantin, G., Tanimoun, B.A., 2016. Model-based study of the role of rainfall and land use–land cover in the changes in the occurrence and intensity of Niger red floods in Niamey between 1953 and 2012. Hydrol. Earth Syst. Sci. 20, 2841–2859. https://doi.org/10.5194/hess-20-2841-2016.

Chen, D., Guo, J., Yao, D., Feng, Z., Lin, Y., 2020. Elucidating the Life Cycle of Warm-Season Mesoscale Convective Systems in Eastern China from the Himawari-8 Geostationary Satellite. Remote Sens 12, 2307. https://doi.org/10.3390/rs12142307.

Chen, X., Leung, L.R., Feng, Z., Yang, Q., 2023. Environmental Controls on MCS Lifetime Rainfall Over Tropical Oceans. Geophys. Res. Lett. 50, e2023GL103267. https://doi.org/10.1029/2023GL103267.

Collischonn, W., Allasia, D., da silva, B.C., Tucci, C.E.M., 2007. The MGB-IPH model for large-scale rainfall—runoff modelling. Hydrol. Sci. J. 52, 878–895. https://doi.org/10.1623/hysj.52.5.878.

CRED-Disaster-Report-Human-Cost2000-2019.pdf, n.d.

Descroix, L., Genthon, P., Amogu, O., Rajot, J.-L., Sighomnou, D., Vauclin, M., 2012. Change in Sahelian Rivers hydrograph: The case of recent red floods of the Niger River in the Niamey region. Glob. Planet. Change 9899 18–30. https://doi.org/10.1016/j.gloplacha.2012.07.009.

Descroix, L., Niang, A.D., Dacosta, H., Panthou, G., Quantin, G., Diedhiou, A., 2013. Évolution des pluies de cumul élevé et recrudescence des crues depuis 1951 dans le bassin du Niger moyen (Sahel). Climatologie 10, 37–49. https://doi.org/10.4267/climatologie.78.

Descroix, L., Guichard, F., Grippa, M., Lambert, L.A., Panthou, G., Mahé, G., Gal, L., Dardel, C., Quantin, G., Kergoat, L., Bouaïta, Y., Hiernaux, P., Vischel, T., Pellarin, T., Faty, B., Wilcox, C., Malam Abdou, M., Mamadou, I., Vandervaere, J.-P., Diongue-Niang, A., Ndiaye, O., Sané, Y., Dacosta, H., Gosset, M., Cassé, C., Sultan, B., Barry, Aliou, Amogu, O., Nka Nnomo, B., Barry, Alseny, Paturel, J.-E., 2018. Evolution of Surface Hydrology in the Sahelo-Sudanian Strip: An Updated Review. Water 10, 748. https://doi.org/10.3390/w10060748.

Di Baldassarre, G., Montanari, A., Lins, H., Koutsoyiannis, D., Brandimarte, L., Blöschl, G., 2010. Flood fatalities in Africa: From diagnosis to mitigation. Geophys. Res. Lett. 37. https://doi.org/10.1029/2010GL045467.

Ding, T., Zhou, T., Guo, Z., Yang, Y., Zou, L., Chen, X., 2024. Contribution of Mesoscale Convective Systems to Floods in the East Asian Summer Monsoon Region. e2023GL108125 Geophys. Res. Lett. 51. https://doi.org/10.1029/2023GL108125.

Feng, Z., Leung, L.R., Houze Jr., R.A., Hagos, S., Hardin, J., Yang, Q., Han, B., Fan, J., 2018. Structure and Evolution of Mesoscale Convective Systems: Sensitivity to Cloud Microphysics in Convection-Permitting Simulations Over the United States. J. Adv. Model. Earth Syst. 10, 1470–1494. https://doi.org/10.1029/2018MS001305.

Feng, Z., Leung, L.R., Hardin, J., Terai, C.R., Song, F., Caldwell, P., 2023. Mesoscale Convective Systems in DYAMOND Global Convection-Permitting Simulations. Geophys. Res. Lett. 50, e2022GL102603. https://doi.org/10.1029/2022GL102603.

Fiolleau, T., Roca, R., 2013. An Algorithm for the Detection and Tracking of Tropical Mesoscale Convective Systems Using Infrared Images From Geostationary Satellite. IEEE Trans. Geosci. Remote Sens 51, 4302–4315. https://doi.org/10.1109/TGRS.2012.2227762.
Fiolleau, T., Roca, R., 2024. A Deep Convective Systems Database Derived from the Intercalibrated Meteorological Geostationary Satellite Fleet and the TOOCAN algorithm (2012–2020). https://doi.org/10.5194/essd-2024-36.
Fiolleau, T., Roca, R., Cloché, S., Bouniol, D., Raberanto, P., 2020. Homogenization of geostationary infrared imager channels for cold cloud studies using Megha-Tropiques/ScaRaB. IEEE Trans. Geosci. Remote Sens 58 (9), 6609–6622. https://doi.org/10.1109/TGRS.2020.2978171.
Fleischmann, A., Siqueira, V., Paris, A., Collischonn, W., Paiva, R., Pontes, P., Crétaux, J.-F., Bergé-Nguyen, M., Biancamaria, S., Gosset, M., Calmant, S., Tanimoun, B., 2018. Modelling hydrologic and hydrodynamic processes in basins with large semi-arid wetlands. J. Hydrol. 561, 943–959. https://doi.org/10.1016/j.jhydrol.2018.04.041.
Geen, R., Bordoni, S., Battisti, D.S., Hui, K., 2020. Monsoons, ITCZs, and the Concept of the Global Monsoon. Rev. Geophys 58, e2020RG000700. https://doi.org/10.1029/2020RG000700.
Gosset, M., Alcoba, M., Roca, R., Cloché, S., Urbani, G., 2018. Evaluation of TAPEER daily estimates and other GPM-era products against dense gauge networks in West Africa, analysing ground reference uncertainty. Q. J. R. Meteorol. Soc. 144, 255–269. https://doi.org/10.1002/qj.3335.
Goyens, C., Lauwaet, D., Schröder, M., Demuzere, M., Van Lipzig, N.P.M., 2012. Tracking mesoscale convective systems in the Sahel: relation between cloud parameters and precipitation. Int. J. Clim. 32, 1921–1934. https://doi.org/10.1002/joc.2407.
Gupta, H.V., Kling, H., Yilmaz, K.K., Martinez, G.F., 2009. Decomposition of the mean squared error and NSE performance criteria: implications for improving hydrological modelling. J. Hydrol. 377 (1-2), 80–91. https://doi.org/10.1016/j.jhydrol.2009.08.003.
Hirabayashi, Y., Kanae, S., Emori, S., Oki, T., Kimoto, M., 2008. Global projections of changing risks of floods and droughts in a changing climate. Hydrol. Sci. J. 53, 754–772. https://doi.org/10.1623/hysj.53.4.754.
Huffman, G.J., Bolvin, D.T., Nelkin, E.J., Tan, J., 2019. Integrated Multi-satellitE Retrievals for GPM (IMERG) Technical Documentation [WWW Document]. URL ⟨https://gpm.nasa.gov/sites/default/files/document_files/IMERG_doc_190909.pdf⟩ (accessed 5.29.24).
Janicot, S., Caniaux, G., Chauvin, F., de Coëtlogon, G., Fontaine, B., Hall, N.M.J., Kiladis, G.N., Lafore, J.-P., Lavaysse, C., Lavender, S.L., Leroux, S., Marteau, R., Mounier, F., Philippon, N., Roehrig, R., Sultan, B., Taylor, C.M., 2011. Intraseasonal variability of the West African monsoon. Atmos. Sci. Lett. 12, 58–66. https://doi.org/10.1002/asl.280.
Kidd, C., Becker, A., Huffman, G.J., Muller, C.L., Joe, P., Skofronick-Jackson, G., Kirschbaum, D.B., 2017. So, how much of the earth's surface is covered by rain gauges? Bull. Am. Meteor. Soc. 98, 69–78. https://doi.org/10.1175/BAMS-D-14-00283.1.
Klein, C., Belušić, D., Taylor, C.M., 2018. WaveleT Scale Analysis of Mesoscale Convective Systems for Detecting Deep Convection from Infrared Imagery. J. Geophys. Res. Atmos. 123, 3035–3050. https://doi.org/10.1002/2017JD027432.
Klein, C., Jackson, L.S., Parker, D.J., Marsham, J.H., Taylor, C.M., Rowell, D.P., Guichard, F., Vischel, T., Famien, A.M., Diedhiou, A., 2021. Combining CMIP data with a regional convection-permitting model and observations to project extreme rainfall under climate change. Environ. Res. Lett. 16, 104023. https://doi.org/10.1088/1748-9326/ac26f1.
Kubota, T., Aonashi, K., Ushio, T., Shige, S., Takayabu, Y.N., Kachi, M., Arai, Y., Tashima, T., Masaki, T., Kawamoto, N., et al., 2020. Global Satellite Mapping of Precipitation (GSMaP) Products in the GPM Era. In: Levizzani, V., Kidd, C., Kirschbaum, D., Kummerow, C., Nakamura, K., Turk, F. (Eds.), Satellite Precipitation Measurement. Advances in Global Change Research, 1st ed., 67. Springer: Berlin/Heidelberg, Germany.
Laipelt, L., de Paiva, R.C.D., Fan, F.M., Collischonn, W., Papa, F., Ruhoff, A., 2025. SWOT reveals how the 2024 disastrous flood in South Brazil was intensified by increased water slope and wind forcing. Geophys. Res. Lett. 52, e2024GL111287. https://doi.org/10.1029/2024GL111287.
Lebel, T., Cappelaere, B., Galle, S., Hanan, N., Kergoat, L., Levis, S., Vieux, B., Descroix, L., Gosset, M., Mougin, E., Peugeot, C., Seguis, L., 2009. AMMA-CATCH studies in the Sahelian region of West-Africa: an overview. J. Hydrol. 375, 3–13. https://doi.org/10.1016/j.jhydrol.2009.03.020.
Maranan, M., Fink, A.H., Knippertz, P., 2018. Rainfall types over southern West Africa: objective identification, climatology and synoptic environment. Q. J. R. Meteorol. Soc. 144, 1628–1648. https://doi.org/10.1002/qj.3345.
Mathon, V., Laurent, H., Lebel, T., 2002. Mesoscale convective system rainfall in the Sahel. J. Appl. Meteor. 41, 1081–1092. https://doi.org/10.1175/1520-0450(2002)041<1081:MCSRIT>2.0.CO;2.
Mohr, K.I., 2004. Interannual, monthly, and regional variability in the Wet Season Diurnal Cycle of Precipitation in Sub-Saharan Africa. J. Clim. 17, 2441–2453. https://doi.org/10.1175/1520-0442(2004)017<2441:IMARVI>2.0.CO;2.
Nash, J.E., Sutcliffe, J.V., 1970. River flow forecasting through conceptual models. Part 1: a discussion of principles. J. Hydrol. 10, 282–290. https://doi.org/10.1016/0022-1694(70)90255-6.
Niger Rapport de situation, 24 sept 2020 | OCHA [WWW Document], 2020. URL https://www.unocha.org/publications/report/niger/niger-rapport-de-situation-24-sept-2020 (accessed 5.29.24).
Panthou, G., Vischel, T., Lebel, T., 2014. Recent trends in the regime of extreme rainfall in the Central Sahel. Int. J. Clim. 34, 3998–4006. https://doi.org/10.1002/joc.3984.
Paris, A., Calmant, S., Gosset, M., Fleischmann, A.S., Conchy, T.S.X., Garambois, P.-A., Bricquet, J.-P., Papa, F., Tshimanga, R.M., Guzanga, G.G., Siqueira, V.A., Tondo, B.-L., Paiva, R., da Silva, J.S., Laraque, A., 2022. Monitoring Hydrological Variables from Remote Sensing and Modeling in the Congo River Basin. In: Congo Basin Hydrology, Climate, and Biogeochemistry. American Geophysical Union (AGU), pp. 339–366. https://doi.org/10.1002/9781119657002.ch18.
Paris, M., n.d. Actualités météo: Pourquoi des inondations catastrophiques au Brésil ? 13/05/2024 [WWW Document]. URL ⟨https://www.meteo-paris.com/actualites/pourquoi-des-inondations-catastrophiques-au-bresil⟩ (accessed 7.4.24).
Pontes, P.R.M., Fan, F.M., Fleischmann, A.S., de Paiva, R.C.D., Buarque, D.C., Siqueira, V.A., Jardim, P.F., Sorribas, M.V., Collischonn, W., 2017. MGB-IPH model for hydrological and hydraulic simulation of large floodplain river systems coupled with open source GIS. Environ. Model. Softw. 94, 1–20. https://doi.org/10.1016/j.envsoft.2017.03.029.
Pontes, P.R.M., Cavalcante, R.B.L., Giannini, T.C., Costa, C.P.W., Tedeschi, R.G., Melo, A.M.Q., Xavier, A.C.F., 2022. Effects of climate change on hydrology in the most relevant mining Basin in the Eastern Legal Amazon. Water 14, 1416. https://doi.org/10.3390/w14091416.
Prein, A.F., Liu, C., Ikeda, K., Bullock, R., Rasmussen, R.M., Holland, G.J., Clark, M., 2020. Simulating North American mesoscale convective systems with a convection-permitting climate model. Clim. Dyn. 55, 95–110. https://doi.org/10.1007/s00382-017-3993-2.
Prein, A.F., Mooney, P.A., Done, J.M., 2023. The multi-scale interactions of atmospheric phenomenon in mean and extreme precipitation. Earths Future 11, e2023EF003534. https://doi.org/10.1029/2023EF003534.
Prein, A.F., Feng, Z., Fiolleau, T., Moon, Z.L., Núñez Ocasio, K.M., Kukulies, J., Roca, R., Varble, A.C., Rehbein, A., Liu, C., Ikeda, K., Mu, Y., Rasmussen, R.M., 2024. Km-scale simulations of mesoscale convective systems over South America—a feature tracker intercomparison. J. Geophys. Res. Atmospheres 129, e2023JD040254. https://doi.org/10.1029/2023JD040254.
Reboita, M.S., Mattos, E.V., Capucin, B.C., Souza, D.Od, Ferreira, G.Wd.S., 2024. A multi-scale analysis of the extreme precipitation in Southern Brazil in April/May 2024. Atmosphere 15, 1123. https://doi.org/10.3390/atmos15091123.
Roca, R., Fiolleau, T., 2020. Extreme precipitation in the tropics is closely associated with long-lived convective systems. Commun. Earth Environ. 1, 1–6. https://doi.org/10.1038/s43247-020-00015-4.
Roca, R., Fiolleau, T., John, V.O., et al., 2024. METEOSAT Long-Term Observations Reveal Changes in Convective Organization Over Tropical Africa and Atlantic Ocean. Surv. Geophys 45, 1979–1998. https://doi.org/10.1007/s10712-024-09862-8.
Schneider, U., Becker, A., Finger, P., Meyer-Christoffer, A., Ziese, M., Rudolf, B., 2014. GPCC's new land surface precipitation climatology based on quality-controlled in situ data and its role in quantifying the global water cycle. Theor. Appl. Clim. 115, 15–40. https://doi.org/10.1007/s00704-013-0860-x.
Sighomnou, D., Descroix, L., Genthon, P., Mahé, G., Bouzou Moussa, I., Gautier, E., Mamadou, I., Vandervaere, J.-P., Bachir, T., Coulibaly, B., Rajot, J.-L., Malam Issa, O., Malam Abdou, M., Dessay, N., Delaitre, E., Maiga, O.F., Diedhiou, A., Panthou, G., Vischel, T., Yacouba, H., Karambiri, H., Paturel, J.-E., Diello, P., Mougin, E., Kergoat, L., Hiernaux, P., 2013. The Niger River Niamey flood of 2012: The paroxysm of the Sahelian paradox? Sécheresse 24, 3–13. https://doi.org/10.1684/sec.2013.0370.

Siqueira, V.A., Paiva, R.C.D., Fleischmann, A.S., Fan, F.M., Ruhoff, A.L., Pontes, P.R.M., Paris, A., Calmant, S., Collischonn, W., 2018. Toward continental hydrologic–hydrodynamic modeling in South America. Hydrol. Earth Syst. Sci. 22, 4815–4842. https://doi.org/10.5194/hess-22-4815-2018.

Taylor, C.M., Belušić, D., Guichard, F., Parker, D.J., Vischel, T., Bock, O., Harris, P.P., Janicot, S., Klein, C., Panthou, G., 2017. Frequency of extreme Sahelian storms tripled since 1982 in satellite observations. Nature 544, 475–478. https://doi.org/10.1038/nature22069.

Todini, E., 1996. The ARNO rainfall—runoff model. J. Hydrol. 175 (1–4), 339–382.

Vogel, P., Knippertz, P., Gneiting, T., Fink, A.H., Klar, M., Schlueter, A., 2021. Statistical forecasts for the occurrence of precipitation outperform global models over Northern Tropical Africa. Geophys. Res. Lett. 48 (3), e2020GL091022. https://doi.org/10.1029/2020GL091022.

Wongchuig, S., Kitambo, B., Papa, F., Paris, A., Fleischmann, A.S., et al., 2023. Improved modeling of Congo's hydrology for floods and droughts analysis and ENSO teleconnections [21 p.] J. Hydrol. Reg. Stud. 50, 101563. https://doi.org/10.1016/j.ejrh.2023.101563.

Zahiri, E.-P., Bamba, I., Famien, A.M., Koffi, A.K., Ochou, A.D., 2016. Mesoscale extreme rainfall events in West Africa: the cases of Niamey (Niger) and the Upper Ouémé Valley (Benin). Weather Clim. Extrem 13, 15–34. https://doi.org/10.1016/j.wace.2016.05.001.

Zhao, M., 2022. A study of AR-, TS-, and MCS-associated precipitation and extreme precipitation in present and warmer climates. J. Clim. 35, 479–497. https://doi.org/10.1175/JCLI-D-21-0145.1.